HEALTH AND MEDICINE

Granzyme B nanoreporter for early monitoring of tumor response to immunotherapy

Anh Nguyen[1], Anujan Ramesh[2]*, Sahana Kumar[1]*, Dipika Nandi[3], Anthony Brouillard[1], Alexandria Wells[3], Leonid Pobezinsky[3,4], Barbara Osborne[3,4], Ashish A. Kulkarni[1,2,3,4]†

Despite recent advancements in cancer immunotherapy, accurate monitoring of its efficacy is challenging due to heterogeneous immune responses. Conventional imaging techniques lack the sensitivity and specificity for early response assessment. In this study, we designed a granzyme B (GrB) nanoreporter (GNR) that can deliver an immune checkpoint inhibitor to the tumor and track time-sensitive GrB activity as a direct way to monitor initiation of effective immune responses. Anti–programmed death-ligand 1 (PD-L1) antibody–conjugated GNRs inhibited PD-1/PD-L1 interactions efficiently and induced T cell–mediated GrB release that can be imaged using activatable imaging probe. GNRs enabled real-time immunotherapy response monitoring in a tumor-bearing mice model and distinguished between highly responsive and poorly responsive tumors. Furthermore, increasing doses resulted in a better response and enhanced sensitivity in poorly responsive tumors. These findings indicate that GNR has the potential to serve as a tool for sensitive and noninvasive evaluation of immunotherapy efficacy.

INTRODUCTION

Recent understanding that tumors co-opt important immune checkpoint pathways, and that blocking of these checkpoints using antibodies unleashes potent antitumor immune response, has transformed cancer immunotherapy (*1*). Immunologic checkpoint blockade therapy using antibodies that target cytotoxic T lymphocyte (CTL)–associated antigen 4 (CTLA-4) and the programmed cell death protein 1 pathway (PD-1/PD-L1) has demonstrated promise in advanced-stage cancers, leading to their approval in a variety of malignancies (*2*). Despite these initial encouraging results, the response has been observed in only a small subset of patients. For example, PD-1 blockade by pembrolizumab induces a response in ~30% of melanoma, 19% of non–small cell lung cancer (NSCLC), 20% of gastric and bladder cancers, and 16% in triple-negative breast cancer (*3*). Similar lower response rates were obtained with PD-L1 antibody treatments (*3*). While combinations of these immune checkpoint inhibitors have shown impressive improvement in efficacy, these approaches are often associated with severe immune-related toxicities due to their different mechanism of action, resulting in distinct toxicity patterns, toxicity kinetics, and dose-toxicity relationships (*4*). These studies suggest that the "one-size-fits-all" immunotherapy approach may not succeed, and early classification of patient responders and nonresponders would be crucial to maximizing the benefits of the cancer immunotherapy.

Standard imaging techniques, including magnetic resonance imaging (MRI), fluorodeoxyglucose–positron emission tomography (FDG-PET), and computed tomography (CT), immune response assays, as well as prognostic and predictive biomarkers, have been shown to be inadequate in accurately predicting and monitoring the initial immune response to immunotherapy (*5*, *6*). Immune checkpoint inhibitor treatments, owing to their unique mechanism of action, are often associated with stromal alterations, resulting in discordant metabolic flux and anatomical changes that result in heterogeneous immune response patterns (*7*). For example, "pseudoprogression" was observed in several patients where either initial increase in tumor burden was later followed by tumor regression or durable shrinkage of target lesion was observed while developing new lesions at other sites (*8*). These response patterns are often misclassified as a progressive disease according to conventional morphological imaging such as MRI. Also, recent studies have shown that FDG-PET or CT is of limited use in this setting (*9*, *10*). Furthermore, transient increase in ^{18}F-FDG uptake during the immunotherapy treatments due to the infiltration of metabolically active inflammatory cells often gives the impression of disease progression (*9*). In addition, recent studies have indicated that the oncogene activation status can regulate the internalization of ^{18}F-FDG (*11*). To address these challenges, several imaging techniques have recently been reported that can monitor the infiltration of T cells in the tumor using PET scans, which are "always-on" imaging systems (*12*–*14*). PET probes have a very short half-life, which makes it difficult to monitor the slower immune response and multiple administrations of PET agents, and frequent imaging needs to be performed. Also, while these techniques can monitor the T cell infiltration in tumors, they cannot discriminate between the cells that have reacted to the tumor (inducing response), in contrast to those that are not responding to the tumor due to immunosuppression and T cell anergy/exhaustion.

The validation of biomarkers could help in predicting responders early on. For example, patients with higher PD-L1 expression or tumor-infiltrating lymphocyte quantity could respond well to PD-L1 therapy, but these markers alone are not sufficient to predict immune response (*15*, *16*). A recent clinical study with PD-L1 antibody (MPDL3280A) suggests that robust responses were observed in some patients with low expression levels of PD-L1 (*17*). Immunohistochemistry (IHC) assays for PD-L1 protein expression have been developed for clinical use. Now, the Food and Drug Administration has approved PD-L1 IHC as a companion diagnostic for anti–PD-1 therapy for patients with NSCLC. Despite this, PD-L1 expression remains an imperfect predictor of Immune Checkpoint

[1]Department of Chemical Engineering, University of Massachusetts, Amherst, MA, USA. [2]Department of Biomedical Engineering, University of Massachusetts, Amherst, MA, USA. [3]Department of Veterinary and Animal Sciences, University of Massachusetts, Amherst, MA, USA. [4]Center for Bioactive Delivery, Institute for Applied Life Sciences, University of Massachusetts, Amherst, MA, USA.
*These authors contributed equally to this work.
†Corresponding author. Email: akulkarni@engin.umass.edu

Inhibitor (ICI) response (*16*). Several assays for measuring immune response (T cell or antibody response) have been developed, but multiple challenges limit their effective use in clinics. For example, in vitro T cell immune response assays are often nonreproducible, which has serious implications for accurately correlating immunological biomarker findings with clinical endpoints such as survival or response (*18*, *19*). Another reason for the lack of correlation between the immune parameters measured and objective clinical response might be the complexity of the immune responses required for a successful tumor eradication, which cannot be dissected through the most frequently used T cell assays (*20*). Also, these assays are mostly carried out on the peripheral blood samples, but recent data suggest that response patterns in the tumors are markedly different than systemic immune responses (*21*). However, the analysis of tumor microenvironment is only restricted to accessible tumors.

Dynamic imaging of immune cell activity after immunotherapy treatment, specifically cytotoxic T cell activity in the tumor microenvironment, could enable direct monitoring of response to cancer immunotherapy and could provide an early indication of the actual response. Also, tracking the cellular level changes, instead of morphological and anatomical changes, can be a more efficient way of differentiating responders from nonresponders early on. Once activated, T cells bind to target cancer cells via T cell receptor (TCR)–major histocompatibility class I (MHC I) and induce apoptosis in the cancer cells by two basic mechanisms: the first one is elicited by granule exocytosis [i.e., perforin and granule-associated enzymes (granzymes)] and the second via the death ligand/death receptor system [Fas Ligand or TNF-related apoptosis-inducing ligand (TRAIL)] (*22*, *23*). Granzyme B (GrB) is one of the most prominent serine proteases involved in the cytotoxic effect of T cells, and monitoring GrB activity will not only allow us to identify the cytotoxic T cells in action but also enable us to quantitatively measure the kinetics of the immune response. To achieve this, we designed a functional activity–based GrB imaging probe where a peptide substrate was conjugated with a fluorescent dye and a quencher pair. Such an activatable imaging probe will allow us to selectively detect the enzyme functions with low false positives and high signal-to-noise ratio as compared to the always-on probes. Furthermore, because T cell–based immune response after immunotherapy treatment and subsequent functional activity of GrB in cancer cells is a time-sensitive process, it is important to deliver the immunotherapy drug and GrB imaging probe to the same cells to efficiently capture the activity. While several recent studies have shown that smart nanoparticle systems can be designed to simultaneously deliver a drug and an imaging agent to the tumor cells (*24*, *25*), to our knowledge, there have been no studies on nanomaterials that can deliver immunotherapy drug and self-monitor GrB activity in real time.

Here, we describe the development of GrB nanoreporter (GNR) that consists of a stimuli-responsive polymer conjugated with an immunotherapy drug and activatable GrB imaging probe (Fig. 1). The GNRs were designed such that they can be used to monitor the GrB activity both in vitro (with a fluorescent dye–quencher pair in the visible range) and in vivo [with a fluorescent dye–quencher pair in the near-infrared (NIR) range]. We demonstrated that GNRs efficiently and selectively monitor GrB activity that correlates well with the T cell activity against cancer cells in an in vitro coculture system. The GNRs were able to distinguish between highly responsive and poorly responsive tumors at lower doses. This correlated very well with significantly higher GrB levels, caspase-3 levels, infiltration of $CD8^+$ T cells, and a higher population of apoptotic cells in the responsive tumors as compared to poorly responsive tumors. In addition, we have shown that GNRs can be used to enhance the imaging efficacy of immunotherapy in poorly responsive tumors at higher doses and at a much earlier time point than the tumor volume measurement without any toxicity. Together, these studies suggest that GNR could emerge as a powerful platform for sensitive, noninvasive, and direct imaging of immunotherapy response.

RESULTS

Rationalization and synthesis of GrB imaging probe

The principal mechanism of CTL-mediated tumor cell killing is the delivery of cytotoxic proteins (granzyme and perforin) to the tumor cell, thereby triggering the caspase-3–mediated apoptosis of the tumor cell (*22*). GrB has been shown to be the most important serine protease (proteins that cleave aspartate residues) required for CTL activity in tumors. We rationalized that monitoring of GrB activity in the tumors in real-time post-immunotherapy treatment could enable direct visualization of immunotherapy response. In this study, we have designed an activatable GrB imaging probe that can track the GrB activity both in vitro and in vivo with higher sensitivity and selectivity than conventional imaging tools and with the maximum signal-to-noise ratio.

The GrB imaging probe was designed using a short peptide that contains a GrB-cleavable Gly-Lys-Ile-Glu-Pro-Asp-Ala-Pro-Cys (GK-IEPD-APC) sequence. The IEPD short peptide sequence was used because it is an established substrate for GrB enzyme (*26*, *27*). This cleavable peptide sequence was conjugated with a fluorescence resonance energy transfer (FRET) pair of either visible-range or NIR fluorophores and quenchers. The visible-spectrum FRET pair consisted of 5-carboxyfluorescein (5-FAM) as a dye (donor) and QSY-7 as a quencher (acceptor). Meanwhile, the NIR-FRET pair included DyLight 755 as donor and DyLight 766Q as an acceptor. We designed the GrB imaging probe with FRET pair in the visible range to elucidate the kinetics of GrB activity in vitro and in the NIR range to enable the noninvasive imaging of GrB activity in vivo. Both visible and NIR pair-tagged enzyme-based cleavage of quenched fluorescent-tagged peptide substrates have been used in tracking different molecular activities of biological systems (*28*). However, these activatable systems have not been used for tracking GrB activity as a direct way to monitor immunotherapy efficacy to the best of our knowledge. The conjugation of the FRET pair to the peptide sequence was accomplished by carbodiimide formation on the lysine and thiol-maleimide coupling on the cysteine. 5-FAM/QSY-7 was chosen as a visible-range FRET pair due to the common use of 488-nm fluorophores in in vitro studies (fig. S1, A and B). Meanwhile, DyLight 755/DyLight 766Q was used as a NIR FRET probe for in vivo experiments to maximize fluorescence signal after activation of the probe when using a NIR small-animal imaging system (fig. S1, C and D). Both visible and NIR FRET pairs have an excellent spectral overlap of donor and acceptor so that the donor fluorophore can transfer its excitation energy to the nearby acceptor in a short distance of less than or equal to 10 nm. These donor-acceptor pairs with excellent spectral overlap when spatially constrained after conjugation to the peptide sequence resulted in maximum quenching efficacies. We first studied the enzymatic susceptibility of the GrB imaging probe by incubating with activated recombinant GrB at 37°C and measured the fluorescence activation after the cleavage

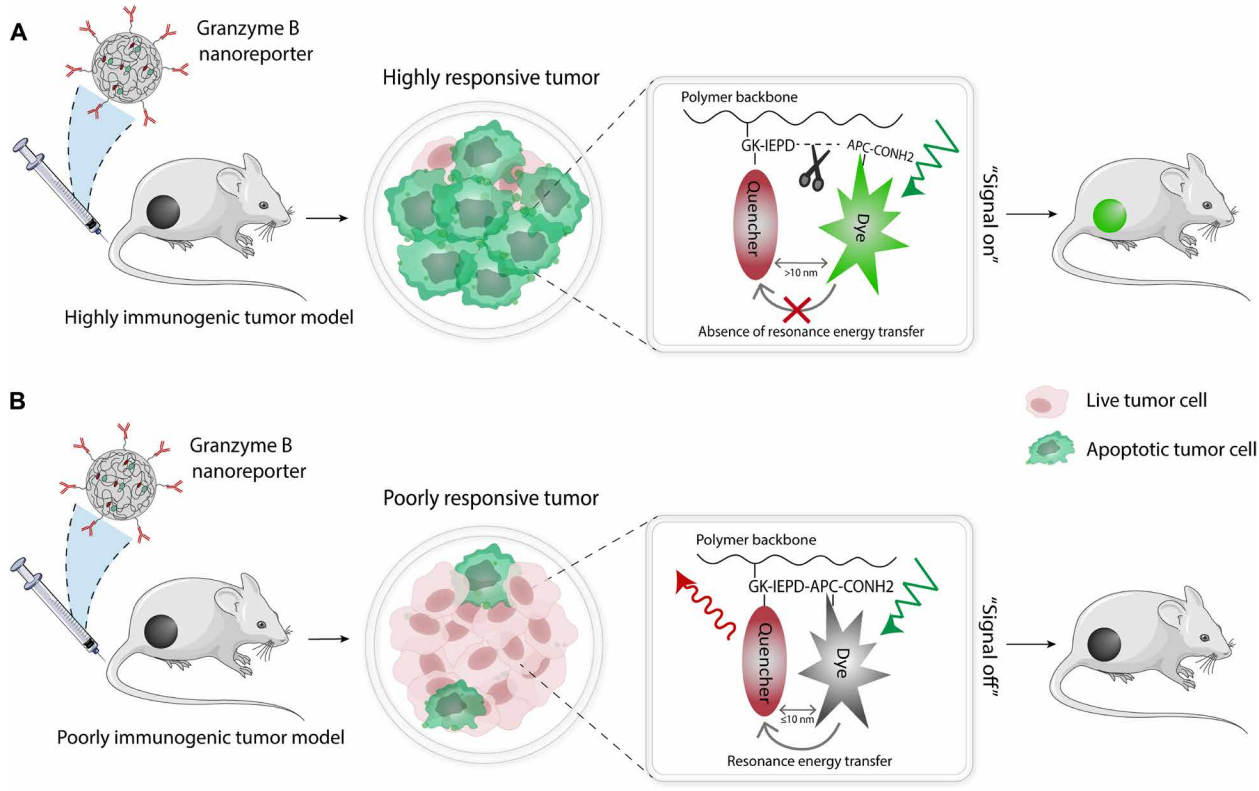

Fig. 1. Schematics showing the mechanism of real-time monitoring of CTL activity using GNRs. GNRs are conjugated with an immune checkpoint inhibitor (anti–PD-L1 antibody) and also carry an activatable imaging probe. The imaging probe consists of a GrB-responsive peptide sequence (GK-IEPD-APC-$CONH_2$) and a dye-quencher pair conjugated on either side of the GrB-cleavable peptide sequence (-IEPD-). When injected intravenously into the tumor-bearing mice, the GNRs accumulate into the tumor, where the binding of an anti–PD-L1 antibody to PD-L1–overexpressing cancer cells results in their internalization. (**A**) In highly immunogenic tumors, this blockade of the PD-L1/PD-1 axis results in cytotoxic T cell–mediated cancer cell killing by the release of GrB. The released GrB cleaves the IEPD sequence and activates the fluorescent signal. (**B**) In the case of poorly immunogenic tumors, partial response resulting from lower cytotoxic T cell activity and lower GrB release fails to activate the fluorescent signal, and the signal remains in the "off" condition. This GrB-mediated fluorescence activation allows direct visualization of the T cell activity in the tumor and can be used to distinguish between immune-responsive and poorly responsive tumors.

of the quenched dye at different time points. As shown in fig. S1E, a gradual increase in the fluorescence intensity was observed over time, resulting in a fourfold increase in fluorescence intensity in 4 hours. Similar results were obtained for the NIR-FRET pair–conjugated GrB imaging probe, which demonstrates that the GrB imaging probes can be used for a range of FRET pairs and can result in activation of the quenched dye after enzymatic cleavage (fig. S1F).

Fabrication and characterization of GNRs

We next synthesized a GNR using three building blocks: a polymer backbone, a GrB imaging probe, and an immunotherapy drug. Poly(isobutylene-*alt*-maleic anhydride) (PIMA) was used as a polymeric backbone to engineer the nanoreporter for several reasons. PIMA is a low-–molecular weight polymer (6 kDa) with highly reactive anhydride functional groups (~40) that could easily be conjugated to different agents without the use of harsh reaction conditions. In a recent study, we have shown that a variety of drugs and imaging probes can be efficiently conjugated to PIMA in an optimized ratio to form self-assembled nanostructures (*28*, *29*). These nanostructures preferentially accumulated into tumors as compared to other organs and exhibited enhanced anticancer efficacy that could be imaged in real time using the imaging probe. It was further demonstrated that the deterministic delivery of drug and drug function–activatable imaging agents using the single nanoparticle enables sensitive imaging of the drug efficacy. We have designed the nanoreporter system in such a way that the immunotherapy drug and GrB imaging probe are delivered using the single nanoparticle to the same cell to maximize the real-time imaging of time-sensitive GrB enzyme activity. To conjugate the anti–PD-L1 antibody to the nanoreporter surface that acts as an immunotherapy drug, we first conjugated carboxy-PEG(8)-amine and GrB imaging probe to PIMA polymer backbone at a molar ratio of 1:9:1 [PIMA:carboxy-PEG(8)-amine:GrB imaging probe] to create a complete polymer construct (fig. S2A). The molar ratio of different components in the polymer construct was optimized to form nanoparticles by self-assembly in aqueous conditions. This was followed by conjugation of the anti–PD-L1 antibody to the polyethylene glycol (PEG)–carboxyl on the nanoparticle surface via standard carbodiimide chemistry to form the GNRs (fig. S2B). To confirm the conjugation of carboxy-PEG(8)-amine and imaging probe to PIMA polymer backbone, we performed proton nuclear magnetic resonance and observed the structural changes in the final construct (fig. S3A). The amount of dye peptide presented in the nanoconstruct was examined using ultraviolet (UV)–visible spectroscopy, and the percentage of imaging probe

after purification was found to be 73.3 ± 8.1% (fig. S3B). We next performed the physiological characterization of the self-assembling GNRs. Transmission electron microscopy (TEM) analysis shows nanoreporters with spherical morphology and an average size of 207 ± 34 nm (fig. S4A). Previous studies have shown that nanoparticles of size ~200 nm can accumulate in solid tumors while escaping liver and spleen filtration (*30*). This advantage imparted because of the enhanced permeability and retention (EPR) effect, where 60- to 500-nm particles can penetrate and maintain at the tumor site (*31*). EPR effect relies on the induced proangiogenic factors and the impaired lymphatic drainage that enhances interstitial fluid pressure to capture extravasated particles (*32*, *33*). Next, we tested the structural stability of GNRs over time by measuring the size and zeta potential using a dynamic light scattering instrument. As shown in fig. S4B, GNRs were shown to be structurally stable for over 7 days during storage conditions at 4°C and in water as measured by changes in size and surface charge. Previous studies have shown that proteins in the biological fluid can rapidly create an adsorption layer of proteins around the surface of nanoparticles in circulation (protein corona), causing the destabilization of nanoparticles (*34*). To evaluate the stability of GNRs in physiologically relevant conditions, the GNRs were incubated in 10% human serum in phosphate-buffered saline (PBS) at 37°C for over 48 hours, and the change in size and zeta potential was monitored over time. We observed no significant change in size and surface charge of GNRs (fig. S4C). This result shows that GNRs are able to maintain the colloidal stability in physiologically mimicking conditions, making them a suitable nanoplatform to deliver immunotherapy drug to the tumor and monitor treatment response. Also, it was found that the zeta potential of GNRs increased with decreasing pH, which indicates the effect of pH environment on the stability of GNRs (fig. S4D). We also conjugated isotype control immunoglobulin G (IgG) antibody on the nanoreporter surface to synthesize control IgG-GNRs, and similar to αPDL1-GNRs, they maintained their stability under the same physiological condition (fig. S5A). Furthermore, NIR-GrB imaging probe–conjugated GNRs exhibited similar physicochemical properties (fig. S5B).

In vitro efficacy and monitoring studies of GNRs

To determine whether the GNRs themselves are toxic to cancer cells, wild type–B16/F10 (WT-B16/F10; hereafter referred to as B16/F10) melanoma cells were incubated with different concentrations of GNRs for 48 hours. As shown in fig. S5C, B16/F10 melanoma cells maintained their viability even at a higher concentration of GNRs. Next, we tested whether the anti–PD-L1 antibody conjugation on the GNRs surface retains its binding to PD-L1 on cancer cells and results in its efficient uptake by the cells. First, B16/F10 cells were treated with interferon-γ (IFN-γ) (20 ng/ml), which resulted in overexpression of PD-L1 on the surface of B16/F10 as compared to untreated cells (fig. S6). Recent studies have shown that IFN-γ secreted from $CD8^+$ T lymphocytes can up-regulate PD-L1 expression on the surface of tumor cells by inducing Janus kinase (JAK)/signal transducer and activator of transcription (STAT) signaling (*35*). These IFN-γ–treated and untreated B16/F10 melanoma cells were then incubated with HiLyte 647–tagged GNRs (far-red dye-tagged GNRs) for 6 hours at 37°C and 5% CO_2 condition. As shown in Fig. 2A, PD-L1–overexpressing B16/F10 cells internalized PD-L1 GNRs at a significantly higher concentration as compared with cells that were not treated with IFN-γ. We further examined different conditions that could affect the internalization of GNRs by cancer cells including different dye tag, time of incubation, and concentration of GNRs. Figure S7A displayed temporal uptake of fluorescein isothiocyanate (FITC)–tagged GNRs (green dye–tagged GNRs) through the endolysosomal pathway. Different concentrations of GNRs incubated with cancer cells also varied the number of internalized GNRs; however, there was no significant difference in uptaking of GNRs between 5 and 10 μM (fig. S7, B and C). Together with the fact that GNRs do not show toxicity to healthy cancer cells at a high concentration of up to 100 μM, all in vitro experiments were conducted with 5 μM GNRs.

We next evaluated the efficacy of GNRs to report on T cell activity in an in vitro setting using WT B16/F10 tumor cells in comparison with B16/F10-OVA. Here, transgenic tumor and T cells were used to direct antigen-specific immune response. Specifically, we hypothesized that upon recognizing specific antigenic peptide by transgenic TCR, a greater T cell–mediated cytotoxicity would eventually augment higher activation of GNRs. This would allow us to differentiate more effectively the antigen-specific (responding) from non–antigen-specific (nonresponding) cytotoxic effect in vitro and evaluate the ability of GNRs to monitor the GrB activity. B16/F10-OVA cells are transfected cells derived from B16/10 melanoma cells that express chicken ovalbumin antigen (OVA). OVA peptide residues are presented on the surface of tumor cells in the context of $H\text{-}2K^b$ MHC class I molecules. For the specific killing of B16/F10-OVA, we used in vitro generated CTLs from OT-I CD8 T cells, where OT-I transgenic TCR recognizes the $OVA_{257–264}$ peptide (SIINFEKL) via the TCR–MHC I interaction. The ability to monitor immune response in real time using GNRs was further evaluated with another set of cells: B16/F10 cells that were loaded with gp33 peptide compared to np396 as the control peptide. Similarly, transgenic P14 TCR on cytotoxic T cells will specifically recognize the lymphocytic choriomeningitis virus (LCMV)–derived gp33–41 peptide presented in the context of $H\text{-}2D^b$ molecules (*36*). All of the experiments with P14 CTLs involved LCMV np396–404 as nonspecific control peptide to compare with gp33–41. P14 CTLs were expected to induce a higher level of apoptosis toward gp33-loaded tumor cells, resulting in the greater fluorescent signal caused by activated GrB probe than np396-loaded cells (*36*).

First, we examined the killing efficacy of antigen-specific $CD8^+$ CTLs toward their targets. As shown in fig. S8, with an increasing number of OT-I T cells in coculture with tumor cells, higher cytotoxic activity against B16/F10-OVA was observed using flow cytometry analysis of propidium iodide (PI) uptake as an indication of cell death. We also observed that when the same ratio of OT-I CTLs to tumor cells was used, significantly lower cytotoxicity was exhibited against B16/F10 (Fig. 2B and fig. S8). We further conducted studies to investigate whether fluorescent activation of the GrB reporter probe delivered by GNRs correlates with the apoptosis in cancer cells (fig. S9A). We first tested the activation of GNRs with different ratios of T cells to B16/F10-OVA by incubating GNRs with tumor cells for 6 hours before differing numbers of OT-I CTLs cells were added. We observed that a 20-fold higher fluorescence signal was detected in the coculture of OT-I CTLs cells and B16/F10-OVA at a ratio of 5:1 compared to 1:5, which correlated with an increase in cell death (Fig. 2C). To explore the ability to monitor apoptosis caused by GrB released from $CD8^+$ T cells in real time, we conducted a time-dependent fluorescence assay when B16/F10-OVA cells were incubated with OT-I CTLs over a period of 24 hours. Not only did

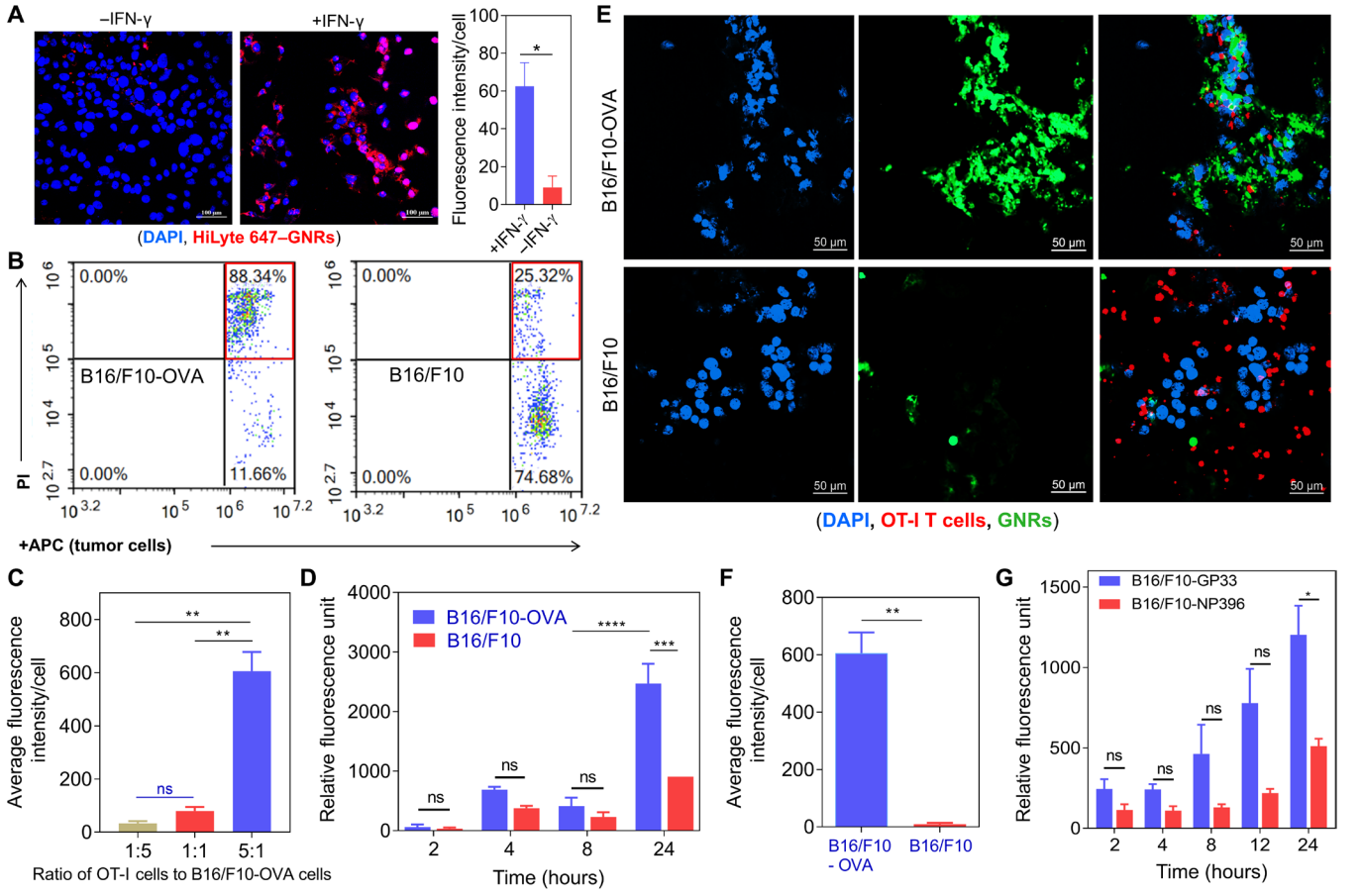

Fig. 2. GNRs enable efficient and selective monitoring of T cell activity against cancer cells in an in vitro coculture system. (**A**) Representative confocal images show internalization of HiLyte 647–tagged GNRs in B16/F10 cells after 6-hour incubation. Cell nuclei were labeled with DAPI (blue), and GNRs were tagged with HiLyte 647 dye (red). Scale bar, 100 μm. Graph shows the quantification of GNR internalization in B16/F10 cells. (**B**) Representative flow cytometry plots show cytotoxic effect of OT-I $CD8^+$ T cells when cocultured with B16/F10 and B16/F10-OVA with a 5:1 ratio of T cells to tumor cells for 24 hours. (**C**) Quantification of fluorescence signal of activated GNRs in coculture of different ratios of OT-I T cells to B16/F10-OVA tumor cells. (**D**) Time-dependent GNR activation when OT-I cells were incubated with either B16/F10 or B16/F10-OVA. (**E**) Representative confocal images show activation of GNRs (green) when B16/F10-OVA cells were cultured with OT-I T cells (red) compared to control B16/F10. Cell nuclei were stained with DAPI (blue). Scale bar, 50 μm. (**F**) Quantification of fluorescence signal of activated GrB probe when OT-I T cells were incubated with cancer cells at a 5:1 ratio. (**G**) Time-dependent measurement of GNR fluorescence intensity in coculture of gp33-coated B16/F10 or control np396-coated B16/F10 cells with P14 T cells. Data in (A), (C), (F), and (G) represent means ± SEM ($n = 3$; ns, no significance; $^*P < 0.05$ and $^{**}P < 0.01$) with Student's *t* test statistical analysis. Data in (D) are means ± SEM ($n = 3$; $^{***}P < 0.001$ and $^{****}P < 0.0001$) using one-way ANOVA followed by Bonferroni post-test.

we observe that fluorescence signal caused by GNRs gradually increased with time in coculture of OT-I CTLs and OVA-expressing tumor cells, but we also showed that GNR activation in B16/F10 cells was significantly lower when there was no specific killing (Fig. 2D). We further confirmed the monitoring efficacy of GNRs by confocal microscopy imaging of coculture of either B16/F10-OVA or B16/F10 cells with OT-I CTLs at a ratio of 5:1 of T cells to targets after 16 to 18 hours, and quantification of the signal was done to confirm the significant difference in fluorescence signal reported by GNRs (Fig. 2, E and F).

Next, we wanted to confirm the monitoring capability of GNRs for cell death caused by cytotoxic T cells using B16/F10 melanoma cells loaded with gp33 and np396 peptides. As shown in fig. S9B, similar cell death pattern was observed when an increasing number of P14 CTLs to the cancer cells was used. However, we observed that the cytotoxic effect of P14 T cells to gp33-loaded B16/F10 was not as high as OT-I T cells to B16/F10-OVA. Despite the overall lower cell death percentage observed in this cytotoxicity assay, GNRs were able to capture the difference in the GrB level released from P14 CTLs to kill the gp33-loaded cells as compared to the control ones. As shown in Fig. 2G and fig. S9C, fluorescence measurement and confocal imaging studies reveal that incubation of GNRs with cancer cells and T cell coculture system results in the time-dependent activation of the GrB fluorescent signal. These studies validate that GNRs could effectively monitor the antigen-specific cytotoxic response of P14 CTLs.

GNRs not only enable early response monitoring but also distinguish between poorly responsive and highly responsive tumors at a lower dose

To test whether GNRs can enable monitoring of anti–PD-L1 treatment in real time, we performed efficacy studies in two different tumor models: WT-B16/F10 melanoma (poorly responsive tumor) and WT-MC38 colon adenocarcinoma tumor (highly responsive tumor). In this set of animal study, we used WT murine C57BL/6

tumor models rather than transgenic ones to maximize the correlation between natural immunogenicity of the two tumor models and the efficacy of therapy. Furthermore, we have chosen B16/F10 because it has been shown to exhibit poorer immunogenicity compared to MC38 tumors in recent studies, resulting in a substandard response to a PD-L1 checkpoint inhibitor (*37*, *38*). On the basis of these observations, we rationalized that the suboptimal dosage of the anti–PD-L1 antibody delivered by GNRs would result in significant cytotoxic T cell response in MC38 tumors as compared to B16/F10 tumors. This activation of the immune response, in turn, would activate the GrB imaging probe in MC38 tumors at a significantly higher degree than in B16/F10 tumors.

To validate this hypothesis, we designed an animal study where C57BL/6 mice were subcutaneously inoculated with MC38 colon adenocarcinoma cells to the right flank and B16/F10 melanoma cells to the left flank of the same mouse. After tumors reached the size of approximately 100 mm^3, tumor-bearing mice were randomly grouped into different GNR treatment groups. Treatment groups included anti–PD-L1–coated GNRs (αPDL1-GNRs), isotype control–coated GNRs (IgG-GNRs), and vehicle. Each dose of GNRs was normalized to deliver 100 μg per mouse equivalent of each antibody and 70 μg per mouse of NIR GrB reporter probe. We hypothesized that the administration of suboptimal doses of 100 μg per mouse would allow us to effectively distinguish the fluorescence signal detected between highly responsive versus poorly responsive tumors on the same animal much earlier than the observed tumor volume changes. The schematic in Fig. 3A shows the design of the study, where injections of treatments were performed on days 0, 2, and 5. Live animal imaging was performed using the In vivo Imaging System (IVIS) every 24 hours after the first injection on day 0. As shown in Fig. 3 (B and C), NIR fluorescence signal due to activation of the GrB imaging probe was detected in MC38 tumors as early as 24 hours after the first dose of αPDL1-GNRs, whereas B16/F10 tumor did not show any detectable signal. The NIR signal was detected as long as 7 days in the MC38 tumors after αPDL1-GNR treatment and was significantly higher than the signal observed in B16/F10 tumors. Control IgG-GNR–treated tumors did not exhibit significant activation of the fluorescence signal in both MC38 and B16/F10 tumors (Fig. 3, B and C). These studies demonstrate that the GNRs not only monitor immunotherapy response in MC38 tumors in real time but also enable distinction in treatment efficacy between B16/F10 and MC38 tumors within the same mice with the systematic injection of the treatment. This also validated the results obtained by recent studies that showed that MC38 responded to anti–PD-L1 treatment with a greater degree than B16/F10 tumors (*38*). Note that these studies used tumor volume measurements or tumor immune components analysis to assess the tumor response to immunotherapy. These methods require a longer time to analyze whether the immunotherapy is working or not because it requires more time to see significant changes in tumor growth inhibition. Also, immune profiling in the tumor requires an invasive procedure to isolate tumor samples or can only be done at the end of the study. However, using GNRs allowed us to noninvasively monitor the response early on as well as for the longer period of time, even before significant tumor volume changes in MC38 and B16/F10 tumors were evident (Fig. 3, D and E). In a recent study by Lin *et al.* (*37*), it was observed that both MC38 and B16/F10 tumors did not show any significant tumor growth inhibition in treatment groups until around 7 days after the first injection of 100 μg of anti–PD-L1 antibody per mouse. A significant difference in the survival rate was observed between MC38 and B16/F10 tumor–bearing mice at the end of day 20 after the first treatment, with MC38 tumor-bearing mice showing better survival profile as compared to B16/F10 tumor–bearing mice. The result was expected, as higher immunogenicity of MC38 tumor allowed a more effective antitumor response. A similar trend of tumor progression was obtained by Juneja *et al.* (*38*) where B16/F10 melanoma tumor was used as a less sensitive model to PD-1/PD-L1 blockade therapy as compared to MC38 colon adenocarcinoma. As shown in Fig. 3F, no notable changes in mice body weights were observed, validating that the GNRs did not exhibit any toxicity. Also, terminal deoxynucleotidyl transferase–mediated deoxyuridine triphosphate nick end labeling (TUNEL) staining of liver tissues from different treatment groups showed no significant levels of apoptotic cells in all the treatments (fig. S10, A and B). In a separate experiment, mice were inoculated with MC38 and B16/F10 tumors on the right and left flanks, respectively, as described previously. The tumors were allowed to reach ≈1000 mm^3 and then administered with a single dose of αPDL1-GNR. After 48 hours, the mice were sacrificed, and the harvested tumors were imaged using an IVIS imaging system (Fig. 4A). The fluorescence signal in MC38 was found to be ~2000% higher as compared with B16/F10 tumor (Fig. 4B). This validates our previous studies where MC38 showed higher activation of fluorescence signal than B16/F10 tumors and the GNRs were able to differentiate between highly responsive versus poorly responsive tumors.

We next evaluated the mechanism of GNR efficacy by performing quantitative analysis of infiltrated T lymphocytes in the tumor microenvironment using flow cytometry. At the end of the study (as described in Fig. 3), the mice were sacrificed, and the tumors were harvested for further mechanistic analysis. As shown in Fig. 4 (C and D), tumor tissues excised from αPDL1-GNR–treated mice showed higher infiltration of $CD8^+$ T cells in MC38 tumor as compared to other groups, but unexpectedly, $CD4^+$ T cells did not show statistically significant infiltration in different treatment groups. MC38 tumors that were treated with vehicle or IgG-GNR control groups showed a basal level of $CD8^+$ T cell infiltration, which was significantly higher than B16/F10 tumors, which validates the fact that MC38 tumors are immunologically active tumors as compared to B16/F10. Next, we wanted to validate that the NIR probe activation in GNRs at the tumor site was due to an increased level of GrB released from activated $CD8^+$ T cells infiltrated in the tumors. Excised tumors were flash-frozen using optimal cutting temperature (OCT) bedding, and tumor tissues were cross-sectioned for further immunofluorescence staining of $CD8^+$ T cells and GrB. As shown in Fig. 4E, the αPDL1-GNR treatment showed the highest infiltration of $CD8^+$ and the highest release of GrB in MC38 tumor as compared with other treatment groups and with B16/F10 tumor sections. Higher infiltration of $CD8^+$ T cells and a higher level of GrB release resulted in significantly higher tumor cell death in MC38 tumors as observed in TUNEL-stained cross sections as compared to B16/F10 tumors (Fig. 4, F and G). Furthermore, comprehensive Western blot analysis showed that αPDL1-GNR treatment resulted in the highest level of GrB and cleaved caspase-3 at the tumor site for both MC38 and B16/F10 compared to IgG-GNR or vehicle groups (Fig. 4, H to J). In addition, in MC38 tumors, both GrB and cleaved caspase-3 were detected at a much greater extent than in B16/F10 tumors, validating the fact that αPDL1-GNRs inhibit the PD-1–PD-L1 axis that results in higher infiltration and activity of $CD8^+$ T cells.

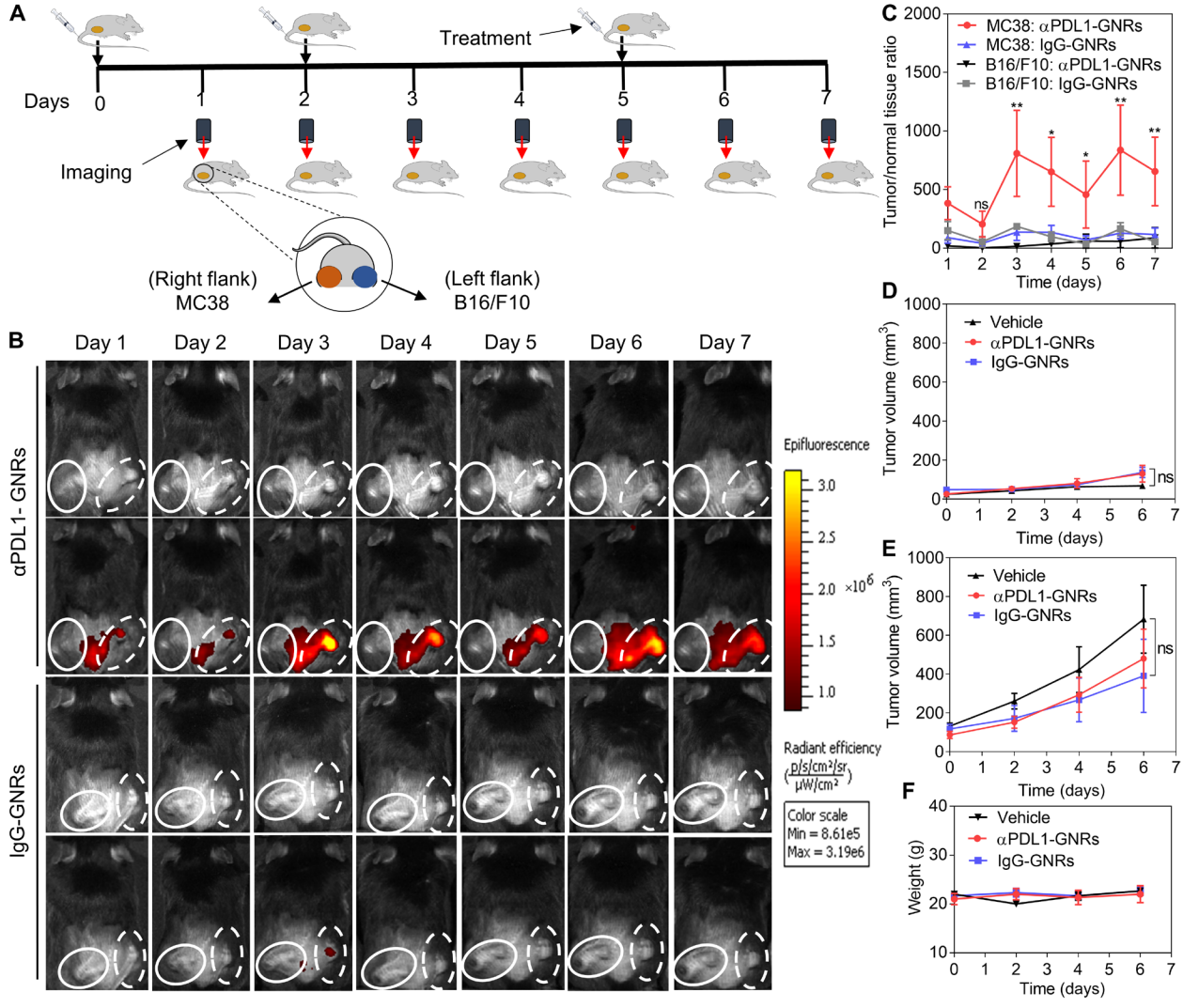

Fig. 3. GNRs enable real-time immunotherapy response monitoring and distinguish between poorly responsive and highly responsive tumors at a lower dose in the C57BL/6 mice model. (**A**) Schematic represents GNR treatment schedule and animal imaging timeline. MC38 tumor (sensitive to anti–PD-L1) and B16/F10 tumor (poorly responsive to anti–PD-L1) were inoculated into the right and left flanks of the same mouse, respectively. After day 7, αPDL1-GNRs (dose equivalent of 5 mg/kg antibody) were injected intravenously into animals, and live mice imaging was performed every 24 hours for 7 days. All the experiments were performed in comparison with isotype control IgG-coated GNR-treated group. (**B**) Representative bright-field and fluorescence images of MC38 (dotted oval) and B16/F10 (solid oval) tumors in mice from different GNR treatment groups, showing time-course fluorescence activation detected by in vivo imaging system (IVIS). (**C**) Quantification of tumor response to different GNR treatments at different time points, as measured by changes in NIR fluorescence intensity in MC38 and B16/F10 tumors and normalized to the fluorescence signal in normal tissues. (**D** and **E**) Treatment efficacy on (D) MC38 and (E) B16/F10 as measured by changes in tumor volume. No statistically significant difference was observed between different treatments in both tumors. (**F**) Changes in overall body weight as an assessment of toxicity of GNR treatments. Data in (C) to (F) are means ± SEM ($n = 3$ to **4**, for each treatment group). Statistical analysis in data (C to E) was determined using one-way ANOVA followed by Bonferroni post-test (*$P < 0.05$ and **$P < 0.01$).

Increasing GNRs dosage allows real-time monitoring of immunotherapy treatment efficacy in poorly responsive tumor

While using suboptimal therapeutic doses allowed us to differentiate the immunotherapy response between highly immunogenic versus poorly immunogenic tumors, we next wanted to check whether the response in poorly immunogenic WT B16/F10 tumors could be enhanced by increasing the GNR dosage. To test this, B16/F10 melanoma tumor–bearing C57BL/6 mice were injected with either αPDL1-GNRs or IgG-GNRs (equivalent dosage of 300 μg per mouse of antibodies and 100 μg per mouse of NIR probe) every alternate day during the study course of 7 days (Fig. 5A). The first live animal imaging was performed 12 hours after the first treatment and then every day after that. With the administration of αPDL1-GNR at a threefold higher dose, significant activation of fluorescence signal was observed in the tumor site as early as 12 hours after the first injection, while there was minimal signal observed in IgG-GNR–injected tumors (Fig. 5, B and C). The fluorescence signal was quantified at all the acquired time points to show the difference in fluorescence signal detected between the two treatment groups (Fig. 5D). The

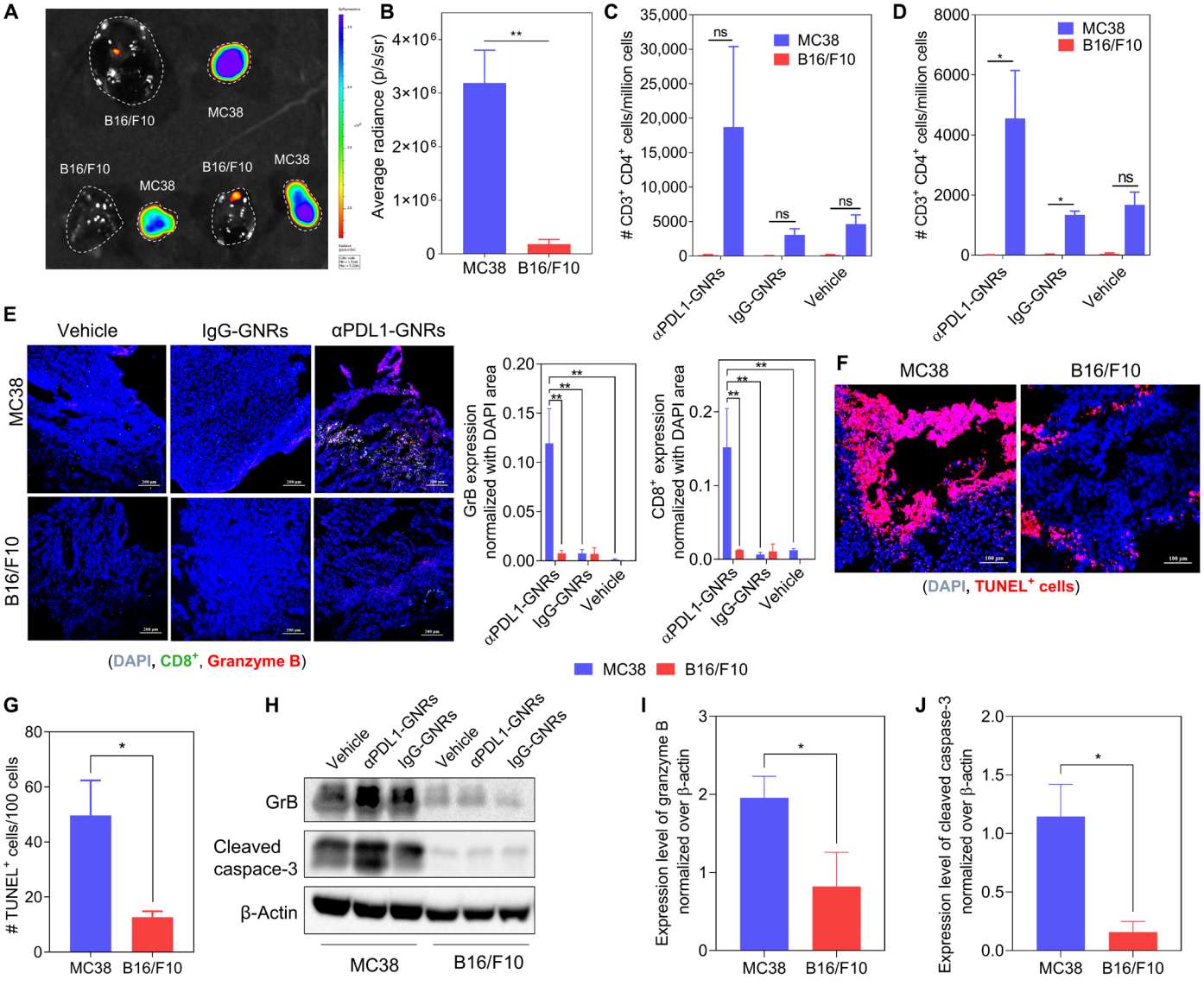

Fig. 4. Ex vivo mechanistic analysis of GNR efficacy in MC38 and B16/F10 tumors. (**A**) Representative NIR fluorescence image of excised MC38 and B16/F10 tumors after a single dose of αPDL1-GNR treatment on day 14 after tumor inoculation; tumors were excised after 48 hours of the treatment. NIR fluorescence was detected and measured using IVIS. (**B**) Quantification of fluorescent signal from (A) using PerkinElmer live imaging software. (**C** and **D**) Quantification of tumor-infiltrating lymphocytes using $CD3^+/CD4^+$ and $CD3^+/CD8^+$ surface markers from single-cell suspension of excised tumors as quantified by flow cytometry. (**E**) Representative confocal images of cross section of excised MC38 and B16/F10 tumors from different treatment groups. Tumor sections were stained for cytotoxic T cell marker CD8a (green) and GrB (red) with DAPI nuclei counterstain (blue). Scale bar, 200 μm. Graphs show quantification of GrB and $CD8^+$ levels in both tumors after different treatments. (**F**) Representative confocal images of tumor sections obtained from αPDL1-GNR treatment that were stained for apoptotic cells using TUNEL staining (red) with DAPI nuclei counterstain (blue). Scale bar, 100 μm. (**G**) Total amount of apoptotic cells from (F). Total $TUNEL^+$ cells (red) were quantified per 100 cells (blue). (**H** to **J**) Western blot analysis shows expression of GrB and cleaved caspase-3 in representative B16/F10 and MC38 tumors from different treatment groups. Data in (B) to (E), (G), (I), and (J) are means ± SEM, and statistical significance was analyzed using Student's *t* test ($n = 3$; $^*P < 0.0$ and $^{**}P < 0.01$).

αPDL1-GNR treatment resulted in a consistently higher activation of the fluorescence signal, which was observed until the end of the study period, whereas IgG-GNR treatment did not show any activation of the fluorescent probe. Also, the spike in the NIR signal was observed in the tumors after each administration of αPDL1-GNR, demonstrating the dose-dependent immunotherapy activity that can be captured using the GrB imaging probe in real time. No significant change in the tumor volumes was observed between the αPDL1-GNR treatment group and control IgG-GNRs, validating the hypothesis that GNRs can enable sensitive immunotherapy response monitoring at much earlier time points than actual tumor volume changes (Fig. 5E). The animal body weights did not show any notable changes, validating that the higher GNR dosage did not exhibit any toxicity to the mice (Fig. 5F). Minimal off-site toxicity of GNRs was further confirmed, as higher doses of GNRs did not exhibit any liver toxicity as shown by TUNEL staining of liver tissues from tumor-bearing mice after different treatments (fig. S10, C and D).

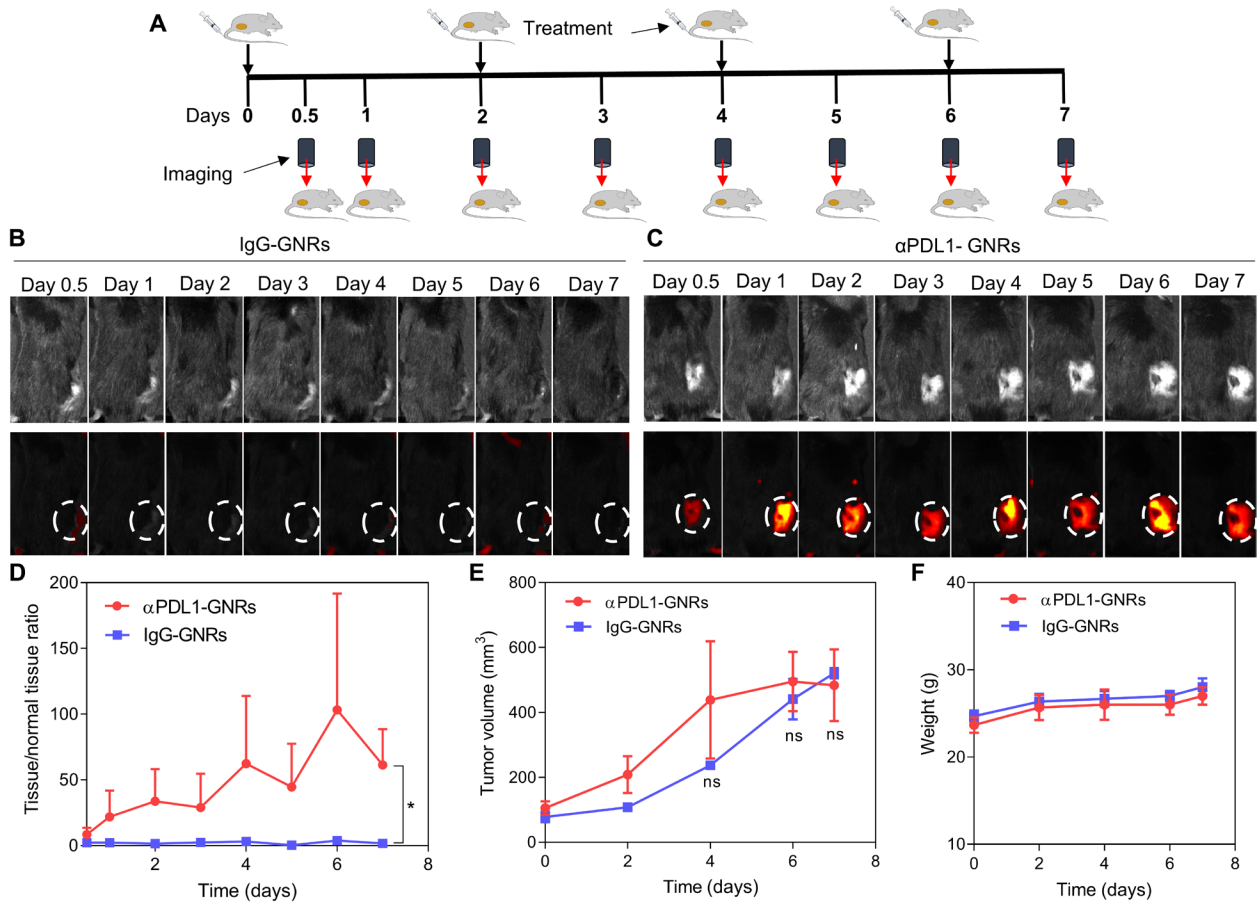

Fig. 5. GNRs monitor immunotherapy response in poorly responsive B16/F10 tumor model at higher dose. (**A**) Schematic shows GNR treatment and imaging schedule. When tumors reached ~500 mm^3, different GNR treatments (αPDL1-GNRs and IgG-GNRs at a dose equivalent of total 15 mg/kg of antibodies) were systematically injected through the tail vein of the mice every alternate day with a total of four doses. Live imaging was performed every 24 hours. (**B** and **C**) Representative fluorescence images of tumors from both treatment groups at different time points using IVIS. (**D**) Quantification of time-dependent tumor response in two treatment groups, as measured by changes in NIR signal in tumors and normalized to normal tissues. (**E**) Efficacy of different GNR treatments on B16/F10 tumors as measured by changes in tumor volumes. (**F**) Different treatments were not toxic to the mice as measured by the change in overall body weight during the course of study. Data in (D) and (E) are means ± SEM, and statistical significance at each respective time point was analyzed using Student's *t* test ($n = 3$; $^*P < 0.05$).

To evaluate the efficacy of GNR treatment to poorly responsive B16/F10 tumor after increasing the dosage of αPDL1-GNR, mechanistic evaluation of the immune status of the tumors was performed. Consistent with previous studies, immunofluorescence staining of tumor cross sections showed higher infiltration of $CD8^+$ T cells in the mice treated with αPDL1-GNRs, resulting in a higher level of GrB at the tumor site as compared to IgG-GNR treatment group (Fig. 6A). This result is consistent with the number of apoptotic cells detected as $TUNEL^+$ signal. As shown in Fig. 6 (B and C), αPDL1-GNR treatment induced a notably greater number of apoptotic cells compared to its control treatment. Flow cytometry data also revealed that αPDL1-GNR treatment resulted in significantly higher infiltration of $CD4^+$ and $CD8^+$ T cells (Fig. 6, D and E). Recent studies have highlighted the fact that natural killer (NK) cells in addition to T cells mediate the immunotherapy effect after PD-1/PD-L1 blockade in some cancers with low MHC expression. As NK cells use similar killing pathway by releasing their cytotoxic granule GrB, we further investigated whether αPD-L1 was specific to enhance immune response caused by infiltrated T lymphocytes. However, no significant difference was observed in the number of NK cells infiltrated into B16/F10 tumors between the two treatment groups (Fig. 6F). We further confirmed the immunotherapy efficacy of GNRs in B16/F10 tumor cells by Western blotting, which revealed an increased level of both GrB and cleaved caspase-3 when mice were treated with αPDL1-GNR instead of the control GNR group (Fig. 6, G to I).

DISCUSSION

Immunotherapy has evolved as a crucial pillar of cancer treatment, and immune checkpoint inhibitors targeting CTLA-4 and PD-1/PD-L1 have produced impressive results in many hard-to-treat cancers (*1*). However, the response remains heterogeneous among patients from different tumor types, with an overall survival benefit occurring in a small number of patients, while inflammatory and other immune-mediated adverse effects resulting from immunotherapy complicate the outcome (*39*). This calls for the identification of robust predictors of response and development of imaging modalities

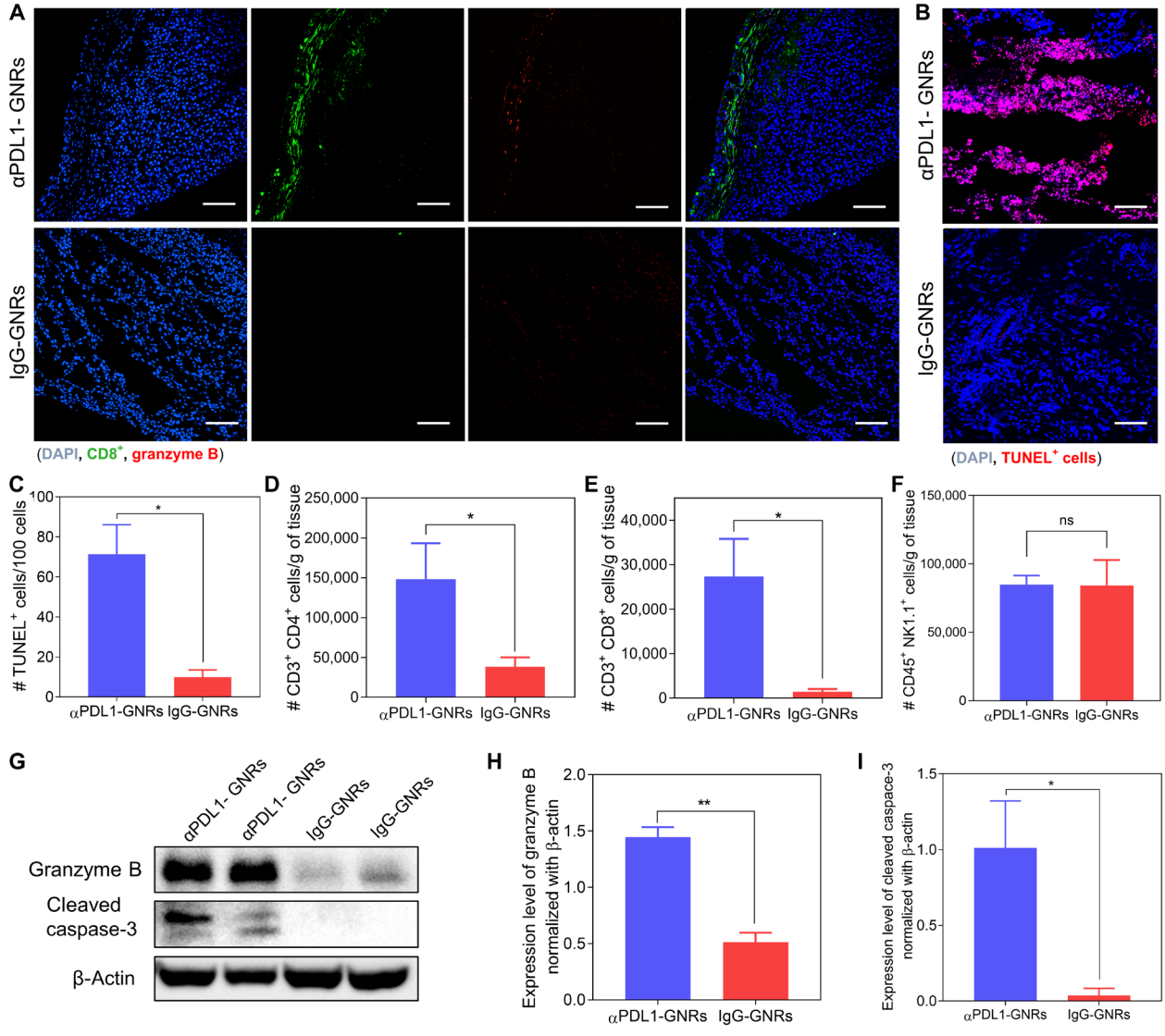

Fig. 6. Mechanistic evaluation of GNR treatment efficacy at higher doses in the B16/F10 tumor model. (**A**) Representative confocal images showing cross sections of excised B16/F10 tumors from αPDL1-GNR and IgG-GNR treatment groups (from the study described in Fig. 5). Tumor sections were stained for CD8a (green) to show infiltrated cytotoxic T cells and apoptotic-mediated granule GrB (red). The cross sections were counterstained with DAPI for nuclei (blue). Scale bar, 100 μm. (**B**) Representative confocal images of B16/F10 tumor sections from both αPDL1-GNR and IgG-GNR treatment groups that were stained for apoptotic cells using TUNEL staining (red). The sections were counterstained with DAPI for nuclei (blue). Scale bar, 100 μm. (**C**) Total amount of apoptotic cells from tumor sections after the treatments. Total $TUNEL^+$ cells (red) were quantified for every 100 cells (blue). (**D** to **F**) Graphs quantifying the amount of infiltration of different effector T lymphocytes using T cell markers ($CD3^+$/$CD4^+$ and $CD3^+$/$CD8^+$) and NK cells ($CD45^+$/$NK1.1^+$) from the single-cell suspension of excised tumors at the end of the study. (**G**) Western blot images of two representative tumors from αPDL1-GNR and IgG-GNR treatment groups show expression of GrB and cleaved caspase-3. (**H** and **I**) Quantification of the expression level of (H) GrB and (I) cleaved caspase-3 from tumor lysates of different GNR treatment groups. Data in (C) to (F), (H), and (I) are means ± SEM ($n = 3$). Statistical significance was determined using Student's *t* test (*$P < 0.05$ and **$P < 0.01$).

for early diagnosis of the treatment effectiveness. Such a tool will help clinicians to ramp up treatments for those patients who are responding and switch quickly to alternative treatments for patients who are not responding, thus avoiding overtreatment and unnecessary toxicity. Recent studies demonstrated that while infiltration of immune cells correlates with immune response, there are no consistent associations between tumor mutational burden, gene mutations, and gene expression patterns with clinical outcomes, making biomarkers for certain cancer types still elusive for immunotherapy (*40*). Also, conventional clinical imaging methods (MRI, CT, ^{18}F-FDG PET), which are used to monitor therapeutic status, cannot differentiate tumor progression from the pseudoprogression that is commonly caused by infiltrated immune cells (*5*, *6*). We have recently demonstrated that ^{18}F-FDG PET/CT imaging was not sensitive to monitor the immunotherapy response in a melanoma mouse model (*28*). In recent studies, a combination of immuno-PET on different biomarkers, $CD8^+$ and $CD11b^+$, was used to track the status of both infiltrated myeloid cells and lymphocytes to better understand their roles in immunotherapy treatment (*12*–*14*, *41*). Ou *et al.* (*42*) designed immunoactive gold nanostars that were able to detect

PD-L1$^+$ and CD8$^+$ signals concurrently in the tumor microenvironment using both Raman reporter and ^{64}Cu radiolabel for PET imaging. While these studies show that correlation of T cell infiltration with therapeutic efficacy may be beneficial in some tumor types, they do not factor in phenomena such as T cell exhaustion, anergy, or the role played by the immunosuppressive tumor microenvironment in repressing T cell activities. Hence, diagnostic approaches that focus on measuring intratumoral T cell activity are required rather than quantifying total immune cell infiltrates that may or may not induce response against tumor cells.

Theranostic systems have been explored as a two-in-one platform for the targeted delivery of both the therapeutic drug and an imaging agent that can simultaneously treat and monitor the status of the nanomaterial delivery in the tumor (*43*, *44*). Previous studies have demonstrated the utility of these theranostic systems in "image-guided therapy" applications including monitoring pharmacokinetics, target site accumulation, drug release profiles at the target site, and off-target accumulation of the nanomaterials (*43*, *44*). However, the always-on aspects of the imaging modalities used in these systems, including PET tracers, MRI agents, and fluorescence dyes, meant that these systems would show signals independent of the drug activity and could not discriminate between drug-responsive versus nonresponsive tumors. Also, while these systems have been explored in delivery and tracking of nanomaterials carrying chemotherapy agents, their use in monitoring immunotherapy response is limited because of delayed and heterogenous response kinetics observed in immunotherapy. Thus, the idea of tracking cellular and molecular level changes after immunotherapy has motivated us to design activatable imaging probes as an effective way to track the immune response.

In this study, we have designed a GNR that can concurrently deliver immunotherapy agents and track the T cell–mediated GrB activity in real time. We rationalized that the real-time monitoring of GrB in the tumor as a marker of T cell activity could enable a more comprehensive examination of tumoral response. Recent studies have shown that GrB expression can be quantitatively correlated to immunotherapy responses and can be used as a biomarker for assessment of therapeutic efficacy (*45*). To accomplish this, we engineered a GNR that contained three components: PIMA polymer as a backbone, anti–PD-L1 immune checkpoint antibodies conjugated to PEG linkers, and a NIR FRET pair conjugated on either side of GrB peptide substrate (-IEPD-). In this study, while we have used PIMA polymer as a backbone to conjugate GrB imaging probe and anti–PD-L1 antibody to synthesize GNRs, extensive toxicity evaluation is warranted to evaluate the potential of this polymer for clinical translation. We have used the peptide sequence (-IEPD-) as a part of a GrB-responsive linker because it has been shown to be selective for this enzyme (*26*, *27*). The optimized molar ratios of each component were used to form a polymer construct. Because of the amphiphilic nature of the polymer construct, it can self-assemble into GNRs, capturing the FRET GrB probe in the core shell while carrying the anti–PD-L1 antibodies on the surface for easier access and binding to PD-L1 ligand–expressing cancer cells. While in this study we have successfully conjugated full-length antibody to GNR surface using 1-ethyl-3-(3-dimethylaminopropyl)carbodiimide (EDC)/*N*-hydroxysuccinimide (NHS) conjugation chemistry, there is a possibility that EDC-NHS coupling may mask the antigen-binding regions of PD-L1 antibody, or the cross-linking of the antibodies due to excess reagents may cause detrimental effects on the binding efficacy and tumor accumulation, as well as penetration and overall pharmacokinetic profiles. Alternatively, the thiol-maleimide coupling can be used. In this report, we validated that activatable GrB imaging is used as a reliable way for early detection of immune checkpoint inhibitors and can be used for longitudinal imaging of the immunotherapy response. Using a tumor model where MC38 colon adenocarcinoma and B16/F10 melanoma tumors were inoculated onto each of its flanks, the GNRs were able to distinguish between the responding and nonresponding tumors. We have used MC38 because it has been demonstrated in recent studies that MC38 tumors respond to immunotherapy treatments with much higher efficiency leading to higher infiltration of T cells and GrB levels in the tumor as compared to B16/F10 tumors (*37*, *38*). This imaging outcome is highly correlated to the quantitative GrB level secreted in tumor tissue, T cell infiltration, and tumor cell death, justifying the ability to determine responders to the treatment by GNRs with exceptional accuracy when no significant divergence in tumor volume could be observed. Moreover, delivering PD-L1 inhibitors and GrB-activatable probe by a single nanocarrier allows capturing the peak of activated fluorescence by synchronizing the spatial and temporal distribution of both therapeutic and reporting elements.

In conclusion, we demonstrated that targeted delivery of immunotherapeutic agent and activatable GrB imaging probe using a nanoreporter can significantly assist in the early determination of effective and ineffective immunotherapy treatments. With the promising results of integrating the GrB biomarker into immunoimaging, this self-reporting platform provides a foundation for translational imaging for anticancer therapy efficacy. Early assessment of cellular activities is therefore a potential application for nuclear imaging to avoid unexpected side effects of ineffective treatment. Furthermore, the reliable correlation between signal quantification from imaging and level of GrB expression allows adjustment of therapy, for example, from single anti–PD-L1 or anti–PD-1 treatment to a combination of anti–PD-L1/PD-1 and anti–CTLA-4. This self-activating imaging platform provides a much earlier and more comprehensive view of the overall immune response after immunotherapy treatments than measurements that depend on changes in anatomical configurations of tumor volume. In addition, the nanoreporter system could also be used as a tool for early monitoring of treatment efficacy in the development of new immunotherapy treatments in future clinical trials.

MATERIALS AND METHODS

Materials

Murine models

All animal experiments were conducted following institutional and national guidelines with established ethics, and all the procedures were approved by the University of Massachusetts Amherst Institutional Use and Care of Animals Committee. C57BL/6 (WT; 4 to 6 weeks) animals were obtained from the Charles River Laboratories to conduct in vivo experiments. Transgenic C57BL/6-Tg(TcraTcrb)1100Mjb/J (stock no. 003831) animals were obtained from The Jackson Laboratory to generate OT-I T cells. B6 Tg(TcrLCMV)327Sdz/JDvs/J P14$^+$ mice were crossed with WT C57BL/6J mice on a Rag2$^{-/-}$ background (The Jackson Laboratory) to generate WT P14$^+$ mice. WT P14$^+$ mice were used to generate P14 T cells. B16/F10 (CRL-6475) melanoma cells were purchased from the American Type Culture Collection. Transduced B16/F10-OVA cells were provided by R. Kamm

(Massachusetts Institute of Technology). MC38 colon adenocarcinoma cells were a gift from B. A. Osborne (Department of Veterinary and Animal Sciences at the University of Massachusetts Amherst). B16/F10 and B16/F10-OVA cells were cultured in Dulbecco's modified Eagle's medium (DMEM; Gibco) supplemented with 10% heat-inactivated fetal bovine serum (FBS) and 1% penicillin-streptomycin (Invitrogen) at 37°C and 15% CO_2 humidified incubator. MC38 colon adenocarcinoma cells were cultured in RPMI 1640 (Gibco) supplemented with 10% FBS, 1% penicillin-streptomycin, 2 mM L-glutamine, 1 mM sodium pyruvate, 0.05 mM 2-mercaptoethanol, and 25 mM Hepes at 37°C humidified incubator maintained at 5% CO_2.

Reagents

Chemical reagents and solvents used in this study were of analytical grade, and there was no further purification before usage. Dichloromethane (DCM), dimethylformamide (DMF), trifluoroacetic acid (TFA), 1,8-diazabicyclo(5.4.0)undec-7-ene (DBU), EDC, *N*-hydroxysulfosuccinimide (Sulfo-NHS), and PIMA were purchased from Sigma-Aldrich. Carboxy-PEG_8-amine was purchased from Thermo Fisher Scientific. 5-FAM and QSY-7 C5-maleimide were purchased from Invitrogen. DyLight 777 maleimide and DyLight 766 NHS ester quencher were purchased from Pierce (Thermo Fisher Scientific). HiLyte 647 amine was purchased from AnaSpec. Deoxyribonuclease I (DNase I) was purchased from Roche. Collagenase type I was purchased from Gibco (Life Technologies). CellTiter 96 AQueous one-solution cell proliferation assay (MTS) was purchased from Promega. Sephadex G-25 was purchased from Sigma Aldrich. 4′,6-Diamidino-2-phenylindole (DAPI) dilactate was purchased from BioLegend. Dialysis tubing was purchased from Spectrum Laboratories. Dynabeads human/mouse T-activator CD3/CD28 was purchased from Thermo Fisher Scientific. The EasySep Human/Mouse T Cell Isolation Kit was purchased from STEMCELL Technologies. IFN-γ and recombinant interleukin-2 (IL-2) carrier-free were purchased from BioLegend. Recombinant mouse GrB enzyme was purchased from BioLegend. All purified and colored antibodies used for in vitro and ex vivo assays were purchased from BioLegend. All isotype controls were used as stated from the manufacturer's instruction. Anti-mouse PD-L1 and rat IgG2b isotype control used from in vivo study were purchased from Bio X Cell. Alexa Fluor 647 goat anti-rat IgG (H+L) was purchased from Invitrogen (Thermo Fisher Scientific). Anti-rabbit goat monoclonal antibody (mAb) Alexa Fluor 594 antibody was purchased from Molecular Probes (Life Technologies). Rabbit anti-mouse GrB, rabbit mAb cleaved caspase-3 antibody, and β-actin antibody were purchased from Cell Signaling Technology. The APC Annexin V Apoptosis Detection Kit with PI was purchased from BioLegend. DMEM and RPMI 1640 (+ L-glutamine) were purchased from Gibco. Reporter elements were characterized using high-performance liquid chromatography (HPLC) with a Gilson GX-271 preparative system and a Bruker ultrafleXtreme matrix-assisted laser desorption/ionization–time-of-flight (MALDI-TOF)/TOF instrument. Nanoparticle hydrodynamic size and zeta potential were measured by dynamic light scattering using Malvern Zetasizer Nano ZSP. Nanoparticle size and morphology were imaged using TEM FEI Tecnai T-12 TEM (Philips). The fluorescence spectrum was measured using a BioTek plate reader. Flow cytometry was conducted using ACEA NovoFlow flow cytometry, and flow data analysis was done using NovoExpress software. Confocal fluorescence images were performed using the Nikon A1 Resonant Scanning Confocal with TIFF Module and Zeiss Spinning Disc Cell Observer SD (Zeiss).

Methods

Reporter element (peptide-FRET) synthesis

GKIEPDAPC-Resin was made following standard Fmoc solid-phase peptide synthesis on a 0.1-mmol scale. Rink amide resin was used as a solid backbone that was first attached to cysteine amino acid. All Fmoc L-amino acids were conjugated to each other following the GKIEPDAPC sequence using N,N′-diisopropylcarbodiimide (DIC) and 1-hydroxy-7-azabenzotriazole (HOAt) coupling agents. Dde protection group on lysine was deprotected using 2% hydrazine in DMF for 10 min. The supernatant was removed, and the removal of Dde was analyzed by UV-visible (UV-vis) spectroscopy. The Dde deprotection step was repeated several times until no more spectrum of Dde was detected by UV-vis spectroscopy. To the IEPD sequence with a free amine group on the lysine, five molar excess of 5-FAM fluorescein dye was used to conjugate to the lysine group through amide bonding. The resin-IEPD sequence with 5-FAM was then cleaved from the solid resin with cleavage cocktail [82.5% trifluoroacetic acid, 5% triisopropylsilane (TIS), 5% deionized water, 5% thioanisole, and 2.5% 3,6-dioxa-1,8-octanedithiol (DODT)], and the peptide was collected by precipitation in ice-cold diethyl ether. The precipitated product was collected by centrifuging at 4000 rpm, and the cold ether was decanted. This step was repeated five more times to completely remove the cleavage mixture from the peptide. The pellet was then dried and lyophilized to form a GK(5-FAM)IEPDAPC-$CONH_2$ with C-terminal amidation and free thiol group on cysteine amino acid. Quencher QSY-7–C5-maleimide was then conjugated to the peptide through a thiol-maleimide reaction in 1 ml of DMF at ambient temperature overnight. The product was then purified using HPLC and lyophilized to obtain a dried pure quenched peptide. The final product was checked for molecular weight using MALDI-TOF mass spectrometry performed on a Bruker ultrafleXtreme MALDI-TOF/TOF instrument. The obtained product was a GrB-cleavable probe with a FRET pair of 5-FAM/QSY-7, where 5-FAM is the donor and QSY-7 is the acceptor, or DyLight 755/DyLight 766, where DyLight 755 is the donor and DyLight 766 is the acceptor.

Activation of GrB reporter probe using GrB enzyme

Recombinant mouse GrB (100 μg/ml) was activated by incubating with active mouse cathepsin C (100 μg/ml) in activation buffer (50 mM MES and 50 mM NaCl; pH 5.5) for 4 hours at 37°C. Activated recombinant mouse GrB was then diluted to 0.5 ng/μl in 200 μM 5,5'-dithiobis-(2-nitrobenzoic acid) (Ellman's Reagent) in assay buffer. Following this, 50 μl of activated GrB enzyme was added to 50 μl of 5-FAM reporter element (50 μM) and allowed to incubate over the course of 4 hours at 37°C in a 96-well plate. Fluorescence intensity was quantified over time, and measurements were recorded every 30 min using a BioTek plate reader at a 5-FAM excitation/emission of 488/520 nm.

GNRs synthesis and characterization

PIMA, 5-FAM or DyLight 755 FRET IEPD sequence, and carboxy-PEG_8-amine with a ratio of 1:9:1 were dissolved in DMF and added together. DBU was added as an organic base to catalyze the reaction. The mixture was stirred at room temperature for 48 hours. After 48 hours of reaction, the resulting sample was dialyzed with a regenerated cellulose dialysis tube with a 1-kDa molecular cutoff size. The mixture was then lyophilized to get a prenanoparticle product. The complete construct of polymer backbone (PIMA) with reporter element and PEG_8-carboxyl was then resuspended in Milli-Q water or PBS, and the mixture was sonicated for 10 min to acquire the

reporter nanoparticles by self-assembly. Anti–PD-L1 or IgG isotype control with free amine group was added to conjugate to PEG_8-carboxyl using 1.5 molar excess of EDC and Sulfo-NHS as coupling agents. The mixture was then gently rocked at 4°C overnight. The resulting nanoparticles were dialyzed or ran through the size-exclusion Sephadex G-25 column. Size and zeta potential were measured by dynamic light scattering using Malvern Zetasizer ZSP. Hydrodynamic change in mean size and colloidal surface charge overtime at 4°C storage conditions were reported as an indication for the physical stability of the nanoparticles. TEM was conducted to measure the morphology of the nanoparticles using FEI Tecnai-T12 (Philips) at cryo. Zeta potential of polymeric nanoparticles incubated at different pH conditions (3.5 and 5.5) was measured using Malvern Zetasizer.

Transmission electron microscopy of GNRs

GNRs were diluted in Milli-Q water and then applied to 400-mesh copper grids. Briefly, 15 μl of the diluted nanoparticle suspension was placed onto the copper grids and allowed to incubate for 30 min. Grids were then wicked with filter paper and allowed to dry for 48 hours. Electron microscopy was performed using a Phillips FEI Tecnai-T12 TEM operating at 120 keV using a TVIPS TemCam-F216 2k by 2k CCD camera system.

In vitro toxicity analysis of polymeric nanoparticles

Blank polymeric nanoparticles (no attached reporter element) were synthesized following the previously described procedure. In short, PIMA and carboxy-PEG_8-amine were added to each other for a reaction in 1 ml of DMF over 48 hours at room temperature. Following this, dialysis was done overnight and lyophilized to obtain a clear thin film. PBS was added to resuspend polymeric film to form nanoparticles at 100 μM concentration (PIMA equivalent) initially with anti–PD-L1 antibody coating. Serial dilution was done to prepare different concentrations of nanoparticles (0.1, 1, 10, and 100 μM); the concentrations correspond to particle abundance. To obtain the desired concentration of particle sample, the $M_1V_1 = M_2V_2$ equation was used, where M_1 is the final concentration for the assay, V_1 is the volume of the culture size, M_2 is the concentration of stock particles, and V_2 is the volume of stock particle suspension. M_1 and V_1 were first determined for each assay to calculate the stock nanomaterial concentration M_2 with $V_2 \cong 0.05\ V_1$ to maintain the living conditions of cells. From M_2 and V_2, the amount of crude nanomaterial was calculated to resuspend with PBS to obtain V_2. B16/F10 melanoma cells were seeded (10×10^3) in a tissue culture 96-well plate and allowed to adhere. Following this, the cells were incubated with nanoparticles over 48 hours at 37°C after 24 hours of being treated with IFN-γ (20 ng/ml). Cells were then washed twice with PBS to remove the media and nanoparticles that were not uptaken by the cells. Cell viability was then measured using an MTS assay kit based on the generation of formazan dye. Formazan dye was quantified using a BioTek plate reader with absorbance measurement at 490 nm.

Internalization study of fluorescent-tagged nanoparticles

B16/F10 melanoma cells (2.0×10^4) were seeded onto an eight-chamber slide system and allowed to adhere. Cells were treated with IFN-γ (20 ng/ml) for 24 hours to up-regulate PD-L1 on the surface of the cells. Cells were washed with 1× PBS and incubated with HiLyte 647– or 5-FAM–tagged PIMA nanoparticles for 1 to 6 hours in a 5% CO_2 atmosphere at 37°C. Cells were fixed using 4% paraformaldehyde and stained for DAPI. Stained cells were mounted using ProLong Glass Antifade Mountant (Invitrogen). Cell slides were imaged using a Nikon A1 resonant confocal microscope. Image analysis was done using NIS Elements 4.6 software.

Isolation of T lymphocytes from mouse spleen and activation of cytotoxic T cells

Spleen was harvested from C57BL/6 mice and disrupted in PBS containing 2% FBS. Single cells were collected and ready for $CD8^+$ isolation. $CD8^+$ was separated following the STEMCELL EasySep Mouse $CD8^+$ T Cell Isolation Kit instruction of either negative or positive selection. Naïve $CD8^+$ mouse T cells were then stimulated to become effector T cells using Dynabeads Mouse T-Activator CD3/CD28 and expanded with mouse IL-2 cytokines (30 U/ml). $CD8^+$ T cells were cultured in Gibco RPMI 1640 supplemented with 10% FBS, penicillin (100 U)–streptomycin (100 μg) (Invitrogen), 10 mM Hepes, 1 mM sodium pyruvate, 2 mM L-glutamine, 1% nonessential amino acids, 0.05 mM 2-mercaptoethanol, and mouse IL-2 (30 U/ml).

Lymph nodes were harvested from WT $P14^+$ mice and gently disrupted to obtain lymphocytes. CD8 T lymphocytes were enriched using antibody-mediated depletion of B cells with anti-mouse IgG magnetic beads (BioMag, Qiagen). CD8 T cells were then stimulated using plate-bound anti-CD28 mAbs (5 μg/ml) and anti-TCRβ mAbs (10 μg/ml). T cells were cultured and differentiated for 5 days in RPMI 1640 (Gibco) supplemented with 10% FBS, 1% penicillin-streptomycin, 10 mM Hepes, 1 mM sodium pyruvate, 2 mM L-glutamine, 1% nonessential amino acids, 0.05 mM 2-mercaptoethanol, and human IL-2 (100 U/ml).

In vitro cell death assay

B16/F10-OVA and B16/F10 were labeled with CellTrace Far Red (CTFR) following the manufacturer's protocol. Labeled cells (2.0×10^4) were added per well in an ultralow attachment round-bottom 96-well plate and cocultured with a different number of activated T cells for 24 hours. Cells in each well were obtained and stained with PI (10 μl/0.5 ml per test) for 15 min at 4°C. Cell death was analyzed using flow cytometry with phycoerythrin (PE)/Texas Red at Ex = 488 nm (PI staining) and allophycocyanin (APC) at Ex = 650 nm (CTFR). Data were analyzed using NovoExpress 1.2.5, where APC and PI^+ cells were gated for the percentage of cell death. In the case of cell death assay performed with P14 T cells, B16/F10 cells were first labeled with CTFR; then, cells were incubated with 1 μM of either LCMV gp33–41or LCMV np396–404 peptide (GenScript) for 1 hour in 5% CO_2 atmosphere at 37°C. Cells coated with np396–404 peptide were referred to as negative control for gp33 cells. Cells were then plated and cocultured with P14 $CD8^+$ cells for 24 hours. PI staining and flow cytometry were performed with the same procedure.

In vitro fluorescence spectra monitoring assay

B16/F10-OVA, B16/F10, gp33-B16/F10, and np396-B16/F10 cells (2.0×10^4) were seeded onto a 96-well black polystyrene microplate with clear bottom (Corning) and allowed to adhere at the bottom of the plate. Cells were then treated with IFN-γ (20 ng/ml) overnight or over 24 hours to induce PD-L1 expression. Cells were washed and incubated with 5 μM αPDL1-GNRs for 6 hours, and $CD8^+$ T cells were added with a 5:1 ratio of T cells to targets at different time points. Tumor cells and T cells were cocultured in complete clear RPMI 1640 at 37°C in 5% CO_2. At the final time point, fluorescence spectra were measured using a BioTek microplate reader at 5-FAM excitation/emission filter.

In vitro fluorescence imaging assay

OT-I and P14 $CD8^+$ T cells were stained with CTFR to distinguish from tumor cells in the coculture. B16/F10-OVA, B16/F10, gp33-B16/F10, and np396-B16/F10 cells (2.0×10^4) were plated in the eight-chamber

slide system and allowed to adhere. Cells were treated with IFN-γ (20 ng/ml) overnight or over 24 hours to up-regulate PD-L1 expression. αPDL1-GNRs (5 μM) were added to the plate for 6 hours, and CTFR-labeled $CD8^+$ T cells were added with different ratios of T cells to targets and incubated for 16 to 18 hours in 5% CO_2 atmosphere at 37°C. At the end of the culture, the chamber slide was fixed with 4% paraformaldehyde and counterstained for nuclei using DAPI. The slide was mounted with ProLong Antifade Mountant (Invitrogen), and fluorescence imaging was performed using Zeiss Spinning Disk. Image analysis was done using Zeiss ZEN software, and quantification of fluorescence was analyzed via ImageJ-Fiji.

In vivo monitoring of GNRs in MC38 and B16/F10 studies

MC38 colon adenocarcinoma cells and B16/F10 melanoma cells (5×10^5) were subcutaneously inoculated into the right and left flanks, respectively, of 4- to 6-week-old C57BL/6 mice weighing around 18 to 20 g (Charles River Laboratories). Tumors were allowed to reach ~100 mm^3, and mice were randomized into different groups. Mice were intravenously injected with either NIR αPDL1-GNRs or NIR IgG-GNRs with a total of 100 μg per mouse of antibodies and 70 μg per mouse of NIR GrB probe to be delivered by nanoparticles in 200 μl of PBS. Treatments were injected at days 0, 2, and 5 of the animal trial. Weight and tumor volume were monitored every alternate day for 7 days after injection. Tumor volume was calculated using the ellipsoid volume formula of $B^2 \times L/2$, with B being the shorter diameter and L being the greater one as measured using a Vernier caliper. Live imaging was done using a PerkinElmer IVIS Spectrum system every 24 hours after the first injection. The stage settings for animal imaging were maintained the same during the entire study. The excitation filter range was set to be 710 to 745, and the emission range was 780 to 820 nm. Fluorescence images of animals were analyzed using PerkinElmer Live Image Software with spectral unmixing, where each signal at the tumor site was separated from autofluorescence. An established spectral library was applied to all raw images for further analysis. The same radiance scale was also kept consistent for the whole analysis, and each relative radiance signal was normalized with background tissue signal. All animal protocols were approved by the University of Massachusetts Institutional Animal Care and Use Committee (IACUC).

In vivo monitoring of GNRs in B16/F10 studies

B16/F10 melanoma cells (1×10^6 cells) were subcutaneously inoculated into the right flanks of 4- to 6-week-old C57BL/6 mice weighing around 18 to 20 g (Charles River Laboratories). At day 10 after tumor inoculation, mice were randomly grouped and NIR GNRs were applied as treatment. The therapy consisted of administration of αPDL1-GNRs and IgG-GNRs; both treatments were administered via the tail vein. The nanoparticles were validated to consist of 100 μg per mouse of responsive NIR GrB probe and 100 μg per mouse of conjugated anti–PD-L1 antibody in 100 μl of PBS. Control IgG nanoparticles were prepared with the equivalent formulation. Additions of 200 μg per mouse of anti–PD-L1 and IgG control antibodies were injected together with prepared reporter nanoparticles. The treatments were injected every alternate day for a total of four dosages per group of animals. Weight and tumor size were measured on the same day of nanoparticle injection until the end of the study. Tumor diameters were monitored with a Vernier caliper, and tumor volume was calculated as ellipsoid volume formula of $B^2 \times L/2$, with B being the shorter diameter and L being the greater one. To conduct imaging on the animal, fluorescence measurement was performed using a PerkinElmer IVIS Spectrum system at the desired time point, starting from 0.5 days after the first injection of treatment. The in vivo NIR fluorescence images were captured and analyzed using Living Image Software with spectral unmixing. All animal protocols were approved by the University of Massachusetts IACUC.

Flow cytometry analysis of excised tumor tissues

At the end of the study, all the mice were sacrificed and tumor from each mouse was harvested. Excised tumors were homogenized in serum-free medium containing collagenase type I (1 mg/ml) and DNase I (0.1 mg/ml) and incubated for 1 hour at 37°C and 5% CO_2. The cells were passed through a 40-μm filter to obtain a single-cell suspension. The single cells were then used to identify the infiltrating lymphocytes by surface staining using APC and FITC anti-mouse antibodies including $CD3^+/CD4^+$, $CD3^+/CD8^+$, and $CD45^+/NK1.1^+$. Antibodies and isotype control concentrations were prepared following the manufacturer's instructions. After staining, cells were washed twice to remove unbound antibodies and analyzed for surface marker using flow cytometry.

Immunofluorescence staining for imaging of $CD8^+$ and GrB in tumor microenvironment

The harvested tumor samples were flash-frozen in Tissue-Tek OCT at −20°C, and frozen tissues were sectioned using a cryostat to obtain 6-μm slices. The tumor sections were fixed with 100% ice-cold methanol or acetone, and permeabilization was done by incubating samples with PBS containing 0.1% Triton X-100 for 10 min. After washing tissue three times with PBS, the samples were incubated with 1% bovine serum albumin (BSA) in PBS containing 0.1% Tween 20 (PBST) for 30 min to block nonspecific binding of antibodies on tumor cells. The sectioned samples were then stained with primary antibodies for CD8a and GrB (rat anti-mouse CD8a and rabbit anti-mouse GrB) at 4°C overnight. Following this, the samples were incubated with desired diluted secondary antibodies (goat anti-rat Alexa Fluor 647 and goat anti-rabbit Alexa Fluor 488) for an hour at room temperature, protected from light. Cell nuclei were counterstained with DAPI with a final concentration of 300 nM (BioLegend). Appropriate PBS washes were done after each step following the standard immunofluorescence staining protocol. The tumor sections were then mounted with ProLong Gold Antifade Mountant. Fluorescence imaging was performed on a Nikon A1R-TIRF confocal microscope, and images were analyzed using NIS Elements 4.6 software.

Ex vivo $TUNEL^+$ signal detection of tissue samples

Tumors and livers were excised and flash-frozen in Tissue-Tek OCT. Frozen samples were sectioned to obtain 6-μm slices using a cryostat. The sections were fixed with 4% paraformaldehyde. Following this, the Click-iT TUNEL Alexa Fluor 594 Assay Kit (Thermo Fisher Scientific) was used to stain for apoptotic cells on the sectioned tissue samples as the manufacturer's protocol. Nuclei of the cells were counterstained with a final concentration of 300 nM DAPI (BioLegend). PBS washes were done between each step to remove excess materials. The sections were then mounted using ProLong Gold Antifade Mountant and covered with glass coverslip. TUNEL images were captured with a Nikon A1R-TIRF confocal microscope and analyzed with NIS Elements v4.6 software and ImageJ-Fiji.

Ex vivo Western blot analysis of tumor tissues

Tumors from all of the mice were excised, and tumor tissues were homogenized in radioimmunoprecipitation assay lysis buffer containing protease and phosphatase inhibitors. The tissue lysate was then centrifuged at 15,000 rpm, and the supernatant was obtained,

followed by protein quantification using the Pierce BCA Protein Assay Kit. An equal amount of 40 μg of protein lysates was mixed with 1× Laemmli SDS sample buffer (Alfa Aesar) and electrophoresed at a constant of 200 V using 10% polyacrylamide gel. The samples were then transferred to polyvinylidene difluoride (PVDF) membrane at a constant current of 35 mA, followed by blocking in tris-buffered saline and 0.1% Tween 20 (TBST) containing 5% skim milk. PVDF membranes were incubated in 1% BSA in TBST with GrB (1:1000 dilution), cleaved caspase-3 (1:1000 dilution), and β-actin (1:2000 dilution) at 4°C for overnight. Appropriate washes with TBST were performed to remove excess antibodies, and membranes were incubated with horseradish peroxidase–conjugated anti-rabbit antibody (1:5000 dilution) in 1% BSA in TBST for 1 hour at room temperature. Bio-Rad's Clarity ECL was used for band detection, and image analysis and quantification were done using Image Lab 6.0.1 and ImageJ 2.0.0.

Statistical analysis

All the data are presented as means ± SEM. Statistical comparison between two groups was performed using a two-tailed Student's *t* test. Statistical analysis among multiple groups was conducted using one-way analysis of variance (ANOVA) followed by Bonferroni post-test. All the statistical analyses were performed using GraphPad Prism 8 software. $P < 0.05$ was considered statistically significant.

SUPPLEMENTARY MATERIALS

Supplementary material for this article is available at http://advances.sciencemag.org/cgi/content/full/6/40/eabc2777/DC1

View/request a protocol for this paper from *Bio-protocol*.

REFERENCES AND NOTES

1. I. Mellman, G. Coukos, G. Dranoff, Cancer immunotherapy comes of age. *Nature* **480**, 480–489 (2011).
2. D. M. Pardoll, The blockade of immune checkpoints in cancer immunotherapy. *Nat. Rev. Cancer* **12**, 252–264 (2012).
3. L. Chen, X. Han, Anti–PD-1/PD-L1 therapy of human cancer: Past, present, and future. *J. Clin. Invest.* **125**, 3384–3391 (2015).
4. R. Zappasodi, T. Merghoub, J. D. Wolchok, Emerging concepts for immune checkpoint blockade-based combination therapies. *Cancer Cell* **33**, 581–598 (2018).
5. J. D. Wolchok, A. Hoos, S. O'Day, J. S. Weber, O. Hamid, C. Lebbé, M. Maio, M. Binder, O. Bohnsack, G. Nichol, R. Humphrey, F. S. Hodi, Guidelines for the evaluation of immune therapy activity in solid tumors: Immune-related response criteria. *Clin. Cancer Res.* **15**, 7412–7420 (2009).
6. M. Nishino, A. Giobbie-Hurder, M. Gargano, M. Suda, N. H. Ramaiya, F. S. Hodi, Developing a common language for tumor response to immunotherapy: Immune-related response criteria using unidimensional measurements. *Clin. Cancer Res.* **19**, 3936–3943 (2013).
7. E. Borcoman, Y. Kanjanapan, S. Champiat, S. Kato, V. Servois, R. Kurzrock, S. Goel, P. Bedard, C. Le Tourneau, Novel patterns of response under immunotherapy. *Ann. Oncol.* **30**, 385–396 (2019).
8. V. L. Chiou, M. Burotto, Pseudoprogression and immune-related response in solid tumors. *J. Clin. Oncol.* **33**, 3541–3543 (2015).
9. C. Sachpekidis, L. Larribere, L. Pan, U. Haberkorn, A. Dimitrakopoulou-Strauss, J. C. Hassel, Predictive value of early ^{18}F-FDG PET/CT studies for treatment response evaluation to ipilimumab in metastatic melanoma: Preliminary results of an ongoing study. *Eur. J. Nucl. Med. Mol. Imaging* **42**, 386–396 (2015).
10. H. Borghaei, L. Paz-Ares, L. Horn, D. R. Spigel, M. Steins, N. E. Ready, L. Q. Chow, E. E. Vokes, E. Felip, E. Holgado, F. Barlesi, M. Kohlhäufl, O. Arrieta, M. A. Burgio, J. Fayette, H. Lena, E. Poddubskaya, D. E. Gerber, S. N. Gettinger, C. M. Rudin, N. Rizvi, L. Crinò, G. R. Blumenschein Jr., S. J. Antonia, C. Dorange, C. T. Harbison, F. Graf Finckenstein, J. R. Brahmer, Nivolumab versus docetaxel in advanced nonsquamous non–small-cell lung cancer. *N. Engl. J. Med.* **373**, 1627–1639 (2015).
11. J. V. Alvarez, G. K. Belka, T.-C. Pan, C.-C. Chen, E. Blankemeyer, A. Alavi, J. S. Karp, L. A. Chodosh, Oncogene pathway activation in mammary tumors dictates FDG-PET uptake. *Cancer Res.* **74**, 7583–7598 (2014).
12. K. V. Keu, T. H. Witney, S. Yaghoubi, J. Rosenberg, A. Kurien, R. Magnusson, J. Williams, F. Habte, J. R. Wagner, S. Forman, C. Brown, M. Allen-Auerbach, J. Czernin, W. Tang, M. C. Jensen, B. Badie, S. S. Gambhir, Reporter gene imaging of targeted T cell immunotherapy in recurrent glioma. *Sci. Transl. Med.* **9**, eaag2196 (2017).
13. M. Rashidian, J. R. Ingram, M. Dougan, A. Dongre, K. A. Whang, C. LeGall, J. J. Cragnolini, B. Bierie, M. Gostissa, J. Gorman, G. M. Grotenbreg, A. Bhan, R. A. Weinberg, H. L. Ploegh, Predicting the response to CTLA-4 blockade by longitudinal noninvasive monitoring of CD8 T cells. *J. Exp. Med.* **214**, 2243–2255 (2017).
14. R. Tavaré, H. Escuin-Ordinas, S. Mok, M. N. McCracken, K. A. Zettlitz, F. B. Salazar, O. N. Witte, A. Ribas, A. M. Wu, An effective immuno-PET imaging method to monitor CD8-dependent responses to immunotherapy. *Cancer Res.* **76**, 73–82 (2016).
15. R. S. Herbst, J.-C. Soria, M. Kowanetz, G. D. Fine, O. Hamid, M. S. Gordon, J. A. Sosman, D. F. McDermott, J. D. Powderly, S. N. Gettinger, H. E. Kohrt, L. Horn, D. P. Lawrence, S. Rost, M. Leabman, Y. Xiao, A. Mokatrin, H. Koeppen, P. S. Hegde, I. Mellman, D. S. Chen, F. S. Hodi, Predictive correlates of response to the anti-PD-L1 antibody MPDL3280A in cancer patients. *Nature* **515**, 563–567 (2014).
16. J. J. Havel, D. Chowell, T. A. Chan, The evolving landscape of biomarkers for checkpoint inhibitor immunotherapy. *Nat. Rev. Cancer* **19**, 133–150 (2019).
17. T. Powles, J. P. Eder, G. D. Fine, F. S. Braiteh, Y. Loriot, C. Cruz, J. Bellmunt, H. A. Burris, D. P. Petrylak, S.-l. Teng, X. Shen, Z. Boyd, P. S. Hegde, D. S. Chen, N. J. Vogelzang, MPDL3280A (anti-PD-L1) treatment leads to clinical activity in metastatic bladder cancer. *Nature* **515**, 558–562 (2014).
18. C. M. Britten, C. Gouttefangeas, M. J. Welters, G. Pawelec, S. Koch, C. Ottensmeier, A. Mander, S. Walter, A. Paschen, J. Müller-Berghaus, I. Haas, A. Mackensen, T. Køllgaard, P. thor Straten, M. Schmitt, K. Giannopoulos, R. Maier, H. Veelken, C. Bertinetti, A. Konur, C. Huber, S. Stevanović, T. Wölfel, S. H. van der Burg, The CIMT-monitoring panel: A two-step approach to harmonize the enumeration of antigen-specific CD8$^+$ T lymphocytes by structural and functional assays. *Cancer Immunol. Immunother.* **57**, 289–302 (2008).
19. S. Janetzki, K. S. Panageas, L. Ben-Porat, J. Boyer, C. M. Britten, T. M. Clay, M. Kalos, H. T. Maecker, P. Romero, J. Yuan, W. M. Kast, A. Hoos; Elispot Proficiency Panel of the CVC Immune Assay Working Group, Results and harmonization guidelines from two large-scale international Elispot proficiency panels conducted by the Cancer Vaccine Consortium (CVC/SVI). *Cancer Immunol. Immunother.* **57**, 303–315 (2008).
20. I. Macchia, F. Urbani, E. Proietti, Immune monitoring in cancer vaccine clinical trials: Critical issues of functional flow cytometry-based assays. *Biomed. Res. Int.* **2013**, 726239 (2013).
21. E. P. Tjin, D. Konijnenberg, G. Krebbers, H. Mallo, J. W. Drijfhout, K. L. Franken, C. M. van der Horst, J. D. Bos, O. E. Nieweg, B. B. Kroon, J. B. Haanen, C. J. Melief, F. A. Vyth-Dreese, R. M. Luiten, T-cell immune function in tumor, skin, and peripheral blood of advanced stage melanoma patients: Implications for immunotherapy. *Clin. Cancer Res.* **17**, 5736–5747 (2011).
22. L. Martinez-Lostao, A. Anel, J. Pardo, How do cytotoxic lymphocytes kill cancer cells? *Clin. Cancer Res.* **21**, 5047–5056 (2015).
23. J. H. Russell, T. J. Ley, Lymphocyte-mediated cytotoxicity. *Annu. Rev. Immunol.* **20**, 323–370 (2002).
24. K. Kim, J. H. Kim, H. Park, Y.-S. Kim, K. Park, H. Nam, S. Lee, J. H. Park, R.-W. Park, I.-S. Kim, K. Choi, S. Y. Kim, K. Park, I. C. Kwon, Tumor-homing multifunctional nanoparticles for cancer theragnosis: Simultaneous diagnosis, drug delivery, and therapeutic monitoring. *J. Control. Release* **146**, 219–227 (2010).
25. K. Y. Choi, G. Liu, S. Lee, X. Chen, Theranostic nanoplatforms for simultaneous cancer imaging and therapy: Current approaches and future perspectives. *Nanoscale* **4**, 330–342 (2012).
26. J. L. Harris, E. P. Peterson, D. Hudig, N. A. Thornberry, C. S. Craik, Definition and redesign of the extended substrate specificity of granzyme B. *J. Biol. Chem.* **273**, 27364–27373 (1998).
27. S. Mahrus, C. S. Craik, Selective chemical functional probes of granzymes A and B reveal granzyme B is a major effector of natural killer cell-mediated lysis of target cells. *Chem. Biol.* **12**, 567–577 (2005).
28. A. Kulkarni, P. Rao, S. Natarajan, A. Goldman, V. S. Sabbisetti, Y. Khater, N. Korimerla, V. Chandrasekar, R. A. Mashelkar, S. Sengupta, Reporter nanoparticle that monitors its anticancer efficacy in real time. *Proc. Natl. Acad. Sci. U.S.A.* **113**, E2104–E2113 (2016).
29. P. Sengupta, S. Basu, S. Soni, A. Pandey, B. Roy, M. S. Oh, K. T. Chin, A. S. Paraskar, S. Sarangi, Y. Connor, V. S. Sabbisetti, J. Kopparam, A. Kulkarni, K. Muto, C. Amarasiriwardena, I. Jayawardene, N. Lupoli, D. M. Dinulescu, J. V. Bonventre, R. A. Mashelkar, S. Sengupta, Cholesterol-tethered platinum II-based supramolecular nanoparticle increases antitumor efficacy and reduces nephrotoxicity. *Proc. Natl. Acad. Sci. U.S.A.* **109**, 11294–11299 (2012).
30. E. Blanco, H. Shen, M. Ferrari, Principles of nanoparticle design for overcoming biological barriers to drug delivery. *Nat. Biotechnol.* **33**, 941–951 (2015).
31. D. A. Scheinberg, C. H. Villa, F. E. Escorcia, M. R. McDevitt, Conscripts of the infinite armada: Systemic cancer therapy using nanomaterials. *Nat. Rev. Clin. Oncol.* **7**, 266–276 (2010).

32. B. Zhang, Y. Hu, Z. Pang, Modulating the tumor microenvironment to enhance tumor nanomedicine delivery. *Front. Pharmacol.* **8**, 952 (2017).
33. S. K. Golombek, J.-N. May, B. Theek, L. Appold, N. Drude, F. Kiessling, T. Lammers, Tumor targeting via EPR: Strategies to enhance patient responses. *Adv. Drug Deliv. Rev.* **130**, 17–38 (2018).
34. P. del Pino, B. Pelaz, Q. Zhang, P. Maffre, G. U. Nienhaus, W. J. Parak, Protein corona formation around nanoparticles—From the past to the future. *Mater. Horiz.* **1**, 301–313 (2014).
35. F. Castro, A. P. Cardoso, R. M. Gonçalves, K. Serre, M. J. Oliveira, Interferon-Gamma at the crossroads of tumor immune surveillance or evasion. *Front. Immunol.* **9**, 847 (2018).
36. A. C. Wells, K. A. Daniels, C. C. Angelou, E. Fagerberg, A. S. Burnside, M. Markstein, D. Alfandari, R. M. Welsh, E. L. Pobezinskaya, L. A. Pobezinsky, Modulation of let-7 miRNAs controls the differentiation of effector CD8 T cells. *eLife* **6**, e26398 (2017).
37. H. Lin, S. Wei, E. M. Hurt, M. D. Green, L. Zhao, L. Vatan, W. Szeliga, R. Herbst, P. W. Harms, L. A. Fecher, P. Vats, A. M. Chinnaiyan, C. D. Lao, T. S. Lawrence, M. Wicha, J. Hamanishi, M. Mandai, I. Kryczek, W. Zou, Host expression of PD-L1 determines efficacy of PD-L1 pathway blockade–mediated tumor regression. *J. Clin. Invest.* **128**, 1708 (2018).
38. V. R. Juneja, K. A. McGuire, R. T. Manguso, M. W. LaFleur, N. Collins, W. N. Haining, G. J. Freeman, A. H. Sharpe, PD-L1 on tumor cells is sufficient for immune evasion in immunogenic tumors and inhibits CD8 T cell cytotoxicity. *J. Exp. Med.* **214**, 895–904 (2017).
39. M. A. Postow, R. Sidlow, M. D. Hellmann, Immune-related adverse events associated with immune checkpoint blockade. *N. Engl. J. Med.* **378**, 158–168 (2018).
40. J. J. Luke, P. A. Ascierto, Biology confirmed but biomarkers elusive in melanoma immunotherapy. *Nat. Rev. Clin. Oncol.* **17**, 198–199 (2020).
41. M. Rashidian, E. J. Keliher, A. M. Bilate, J. N. Duarte, G. R. Wojtkiewicz, J. T. Jacobsen, J. Cragnolini, L. K. Swee, G. D. Victora, R. Weissleder, H. L. Ploegh, Noninvasive imaging of immune responses. *Proc. Natl. Acad. Sci. U.S.A.* **112**, 6146–6151 (2015).
42. Y.-C. Ou, X. Wen, C. A. Johnson, D. Shae, O. D. Ayala, J. A. Webb, E. C. Lin, R. C. DeLapp, K. L. Boyd, A. Richmond, A. Mahadevan-Jansen, M. Rafat, J. T. Wilson, J. M. Balko, M. N. Tantawy, A. E. Vilgelm, R. Bardhan, Multimodal multiplexed immunoimaging with nanostars to detect multiple immunomarkers and monitor response to immunotherapies. *ACS Nano* **14**, 651–663 (2020).
43. T. Lammers, S. Aime, W. E. Hennink, G. Storm, F. Kiessling, Theranostic nanomedicine. *Acc. Chem. Res.* **44**, 1029–1038 (2011).
44. F. M. Kievit, M. Zhang, Cancer nanotheranostics: Improving imaging and therapy by targeted delivery across biological barriers. *Adv. Mater.* **23**, H217–H247 (2011).
45. B. M. Larimer, E. Wehrenberg-Klee, F. Dubois, A. Mehta, T. Kalomeris, K. Flaherty, G. Boland, U. Mahmood, Granzyme B PET imaging as a predictive biomarker of immunotherapy response. *Cancer Res.* **77**, 2318–2327 (2017).

Acknowledgments: We would like to acknowledge the support and assistance of the Biophysical Characterization Core Facility, Light Microscopy Core Facility, and Animal Imaging Facility at the Institute for Applied Life Sciences (IALS) and the Electron Microscopy Core Facility at the University of Massachusetts Amherst. **Funding:** This work was financially supported by the American Cancer Society Research Scholar Grant (RSG-19-009-01-CDD), Melanoma Research Alliance Young Investigator Award (510283), and Cancer Research Institute Technology Impact Award (118-1501) to A.A.K. and NIH grant (R01 AI146188) to L.P. **Author contributions:** A.A.K. conceived and supervised the project. A.N. and A.A.K. designed the experiments. A.N., A.R., S.K., D.N., and A.B. performed the experiments and analyzed the data. A.W. and L.P. provided the P14 cells. L.P. and B.O. provided inputs in the T cell–based assays. A.N. and A.A.K. wrote the manuscript. All the authors read and approved the manuscript. **Competing interests:** A.A.K. is an inventor on a patent application filed by Brigham and Women's Hospital (no. 62/302,435, filed on 2 March 2016). The authors declare no other competing interests. **Data and materials availability:** All data needed to evaluate the conclusions in the paper are present in the paper and/or the Supplementary Materials. Additional data related to this paper may be requested from the authors.

Submitted 15 April 2020
Accepted 14 August 2020
Published 2 October 2020
10.1126/sciadv.abc2777

Citation: A. Nguyen, A. Ramesh, S. Kumar, D. Nandi, A. Brouillard, A. Wells, L. Pobezinsky, B. Osborne, A. A. Kulkarni, Granzyme B nanoreporter for early monitoring of tumor response to immunotherapy. *Sci. Adv.* **6**, eabc2777 (2020).